Magmatic Origins of Extensional Structures in Tempe Terra, Mars

Claire Jennifer Orlov[1], Emma K Bramham[1], Paul K. Byrne[2], Sandra Piazolo[3], and Mark Thomas[1]

[1]University of Leeds
[2]Washington University in St. Louis
[3]School of Earth and Environment, The University of Leeds

June 14, 2023

Abstract

Numerous graben features transect the Tempe Terra plateau in the northeastern Tharsis Rise, making it one of the most heavily structured regions of Tharsis. The origin of the complex fault geometries, generated over three distinct stages of tectonic activity, is still poorly understood. This work distinguishes between locally-sourced and regionally-sourced structures within Tempe Terra, to isolate regional deformation patterns related to the general development of the Tharsis Rise from the effects of local mechanisms. Comparison of structural observations to predicted deformation patterns from different sources of graben formation in the Martian crust demonstrates the important role of magmatic activity at a variety of scales in driving tectonism in Tempe Terra. Noachian (Stage 1) faulting was the result of local magmatic underplating and associated heating and uplift, which formed part of an incipient stage of widespread Tharsis volcanism that predated development of the main Tharsis Rise. Early Hesperian (Stage 2) faults reflect the interaction of regional stresses from growth of the Tharsis Rise with magmatic activity highly localised along the Tharsis Montes Axial Trend – a linear volcanotectonic trendline including the alignment of the Tharsis Montes volcanoes. Early–Late Hesperian (Stage 3) faulting resulted from a series of dyke swarms from a Tharsis-centred plume, which propagated in a regional stress field generated by growth of the Tharsis Rise. As only Stage 2 NNE faults and Stage 3 ENE faults are linked to regional, Tharsis-related stresses, other observed Tempe Terra fault trends can be excluded when evaluating models of Tharsis's tectonic evolution.

Hosted file

`965509_0_art_file_11067074_rvw90b.docx` available at https://authorea.com/users/555565/articles/648496-magmatic-origins-of-extensional-structures-in-tempe-terra-mars

Magmatic Origins of Extensional Structures in Tempe Terra, Mars

C. J. Orlov[1], E.K. Bramham[1], P.K. Byrne[2], S. Piazolo[1], and M. Thomas[1]

[1]School of Earth and Environment, University of Leeds.

[2]Department of Earth and Planetary Sciences, Washington University in St. Louis.

Corresponding author: Claire Orlov (eecjo@leeds.ac.uk)

Key Points

- The 3 stages of Tempe Terra's tectonic activity have different origins, with local and regional scale magmatic sources driving deformation
- Magmatectonic activity began in Tempe Terra prior to development of the Tharsis Rise topographic bulge and associated major volcanoes
- Only 2 Tempe Terra fault trends, both Hesperian age, represent stresses related to the growth of Tharsis: NNE (Stage 2) and ENE (Stage 3)

Abstract

Numerous graben features transect the Tempe Terra plateau in the northeastern Tharsis Rise, making it one of the most heavily structured regions of Tharsis. The origin of the complex fault geometries, generated over three distinct stages of tectonic activity, is still poorly understood. This work distinguishes between locally-sourced and regionally-sourced structures within Tempe Terra, to isolate regional deformation patterns related to the general development of the Tharsis Rise from the effects of local mechanisms. Comparison of structural observations to predicted deformation patterns from different sources of graben formation in the Martian crust demonstrates the important role of magmatic activity at a variety of scales in driving tectonism in Tempe Terra. Noachian (Stage 1) faulting was the result of local magmatic underplating and associated heating and uplift, which formed part of an incipient stage of widespread Tharsis volcanism that predated development of the main Tharsis Rise. Early Hesperian (Stage 2) faults reflect the interaction of regional stresses from growth of the Tharsis Rise with magmatic activity highly localised along the Tharsis Montes Axial Trend – a linear volcanotectonic trendline including the alignment of the Tharsis Montes volcanoes. Early–Late Hesperian (Stage 3) faulting resulted from a series of dyke swarms from a Tharsis-centred plume, which propagated in a regional stress field generated by growth of the Tharsis Rise. As only Stage 2 NNE faults and Stage 3 ENE faults are linked to regional, Tharsis-related stresses, other observed Tempe Terra fault trends can be excluded when evaluating models of Tharsis's tectonic evolution.

Plain Language Summary

Tharsis is the largest volcanic province on Mars and its formation was a major driver of the deformation we see at the surface. Tectonic structures are therefore used to understand how and when Tharsis formed. However, local structural patterns may obscure regional trends associated with Tharsis-forming stresses, complicating our ability to assess models for how Tharsis developed. As such, distinguishing between faults with local and regional origins is essential. Here, we study the Tempe Terra region in northeastern Tharsis to determine the origin of the region's extensive faulting, generated over three distinct stages of tectonic activity. By comparing surface observations to expected evidence of different sources of stress, such as uplift from local volcanoes or dyke intrusion, we found that each stage of tectonic activity had a different origin. A combination of local scale (from within Tempe Terra) and regional scale (from Tharsis) magmatic sources drove deformation, and tectonic activity began before the main structures and volcanoes of Tharsis had developed. Only two fault trends in Tempe Terra can be linked to regional stresses related to the

growth of Tharsis: NNE-trending and ENE-trending faults. Isolating these regional trends provides clearer criteria for assessing models of Tharsis development in the future.

1 Introduction

The development of the Tharsis Rise is suggested to be a major driver of planetary-scale deformation and structural processes on Mars (Banerdt et al., 1992; Golombek & Phillips, 2010). However, the fundamental mechanisms responsible for this development remain disputed, with proposed models including isostasy, flexure, mantle plume uplift, and dynamic mantle support (e.g., Baker et al., 2007; Banerdt et al., 1982; Mège & Masson, 1996a; Solomon & Head, 1982; Tanaka et al., 1991). Surface deformation patterns can tell us about the timing, nature, and orientation of stress regimes, and form a primary source of evidence for interpreting the timing and mechanism of Tharsis's development. Extensive systems of radiating normal faults and circumferential wrinkle ridges (the surface expression of thrust faults) are centred on the topographic bulge of the Tharsis Rise (Figure 1a). Since these observed structures have been primarily attributed to Tharsis's growth and activity through time, faults patterns have been used to constrain and/or test various models of Tharsis development (e.g., Anderson et al., 2001; Banerdt et al., 1982; Dohm et al., 2007; Mège & Masson, 1996a; Tanaka et al., 1991). However, the surface deformation around Tharsis is often highly complex and can vary significantly in character across the region, with the potential for multiple overprinting effects in different locations. Therefore, to fully utilise the surface deformation features and provide the most accurate criteria for Tharsis models, a two step evaluation is needed. First, we need to distinguish between features formed as a result of Tharsis-related regional stress fields or magmatic processes, and those related to local processes and heterogeneities. Second, locally-sourced structures should be excluded from assessments of regional-scale stress. This process of isolating regional patterns from local complexities may help to further clarify the mechanisms of Tharsis's development.

Here, we distinguish between faults with local and regional origins in one of the most heavily faulted areas of Tharsis: Tempe Terra (Figure 1a). Tempe Terra's structural complexity can provide important information regarding Tharsis's development. Its location has allowed preservation of older rocks and structures which have been buried by younger lava flows in most other areas in the northern half of Tharsis. It consists of a plateau dominated by extensional structures, mostly in the form of graben, with complex patterns of crosscutting faults. Tempe Terra also lies along the "Tharsis Montes Axial Trend" (Figure 1a), an alignment of volcanoes and extensional structures along a single great circle stretching over 6500 km through the centre of the Tharsis Rise, including the three Tharsis Montes volcanoes and the Tempe Rift system in Tempe Terra (Carr, 1974; Hauber &

Kronberg, 2001; Wise et al., 1979). The scale and striking linear nature of this trend indicate it is significant in the geological history of the Tharsis Rise, and may be controlled by some pre-Tharsis structure (e.g. Carr, 1974; Schultz, 1984; Wise et al., 1979).

Orlov et al. (2022) identified three primary stages of tectonic activity in Tempe Terra, spanning from the Middle Noachian to Late Hesperian (Figure 1). The origin of these specific stages has not yet been defined, and the complexity of Tempe Terra's fault patterns has not been reflected in previous assessments of formation mechanisms for these faults. Outside of a general association with stress from Tharsis (e.g. Hauber et al., 2010; Tanaka et al., 1991; Wise et al., 1979), the origin of extension in Tempe Terra has not previously been examined in the detail required to explain the observed differences in structural character through time. Past studies have suggested faulting in Tempe Terra is a result of dyke intrusion (e.g. Davis et al., 1995; Mège & Masson, 1996a) or volcanic rifting (Hauber & Kronberg, 2001; Mège et al., 2003), with later interpretation proposing oblique rifting for the Tempe Rift (Fernández & Anguita, 2007). However, these studies have typically applied a single interpretation for all of Tempe Terra's faults, or have investigated only the Tempe Rift, which is insufficient to distinguish between locally-sourced and regionally-generated deformation.

This study aims to determine the origin of extensional faults produced during each stage of Tempe Terra's tectonic development, to better understand the interplay of local and regional mechanisms and ultimately shed light on processes associated with Tharsis's development. This work builds upon the foundation of geometric observations and age assignments from Orlov et al. (2022) to extract the origin of specific structural trends through time. Our approach analyses fault data and associated features from each stage to identify surface evidence of different sources of extensional stress and graben formation in the Martian crust. To further expand on this analysis and understand the complexities involved in interpretation, we also investigate the likelihood of fault reactivation throughout the evolution of Tempe Terra. We are then able to extract regionally-relevant trends and consider their implication for future models of Tharsis's evolution.

1.1 Geological background and tectonic stages of Tempe Terra

Tempe Terra is a large plateau (~2 million km^2) of Noachian and Hesperian volcanic and highland units (Tanaka et al., 2014) at the NE edge of the Tharsis Rise (Figure 1a). Over 23,700 normal faults have been mapped across Tempe Terra and separated into sixteen fault sets based on their age and orientation (Orlov et al., 2022). These faults range in age from Middle Noachian to Amazonian but the majority of tectonic activity occurred in Tempe Terra during the Early Hesperian (Figure 1; Orlov et al., 2022). The fault sets are separated into three stages, each with a different primary orientation. Each stage represents a continuous period where tectonic features had a similar alignment and spatial distribution, before a resolvable shift in fault patterns is observed in the relative timeline. Stage 1 (Middle Noachian to Early Hesperian) consists of predominantly N-trending graben with minor NW-trending structures which together comprise seven fault sets (Figure 1b). These faults are contained to the western half of Tempe Terra. Stage 2 (Early Hesperian) consists of NNE- to NE-trending normal faults across three fault sets (Figure 1c). Structures from this stage form a localized zone of high fault spatial density through the centre of Tempe Terra and form the Tempe Rift system. Stage 3 (Early Hesperian to Late Hesperian) consists of ENE-trending graben from five fault sets (Figure 1d). These faults are distributed across the full width of the plateau.

Figure 1: Tempe Terra in the context of the Tharsis Rise. **a)** Western hemisphere of Mars showing the Tharsis Rise, Tharsis Montes Axial Trend, and extensional and shortening structures from Tanaka et al. (2014). Additional graben axes in Tempe Terra subsampled from Orlov (2022). UM = Uranius Mons, SM = Sirenum Mons, ST = Sirenum Tholus. **b–d)** Fault set maps of Tempe Terra for each tectonic stage from Orlov et al. (2022). Fault set names and associated colours for each stage are shown on each image, with all other Tempe Terra faults shown in grey. Ages and relative timing of fault sets are shown on timeline. Background to all images is shaded relief HRSC–MOLA DEM.

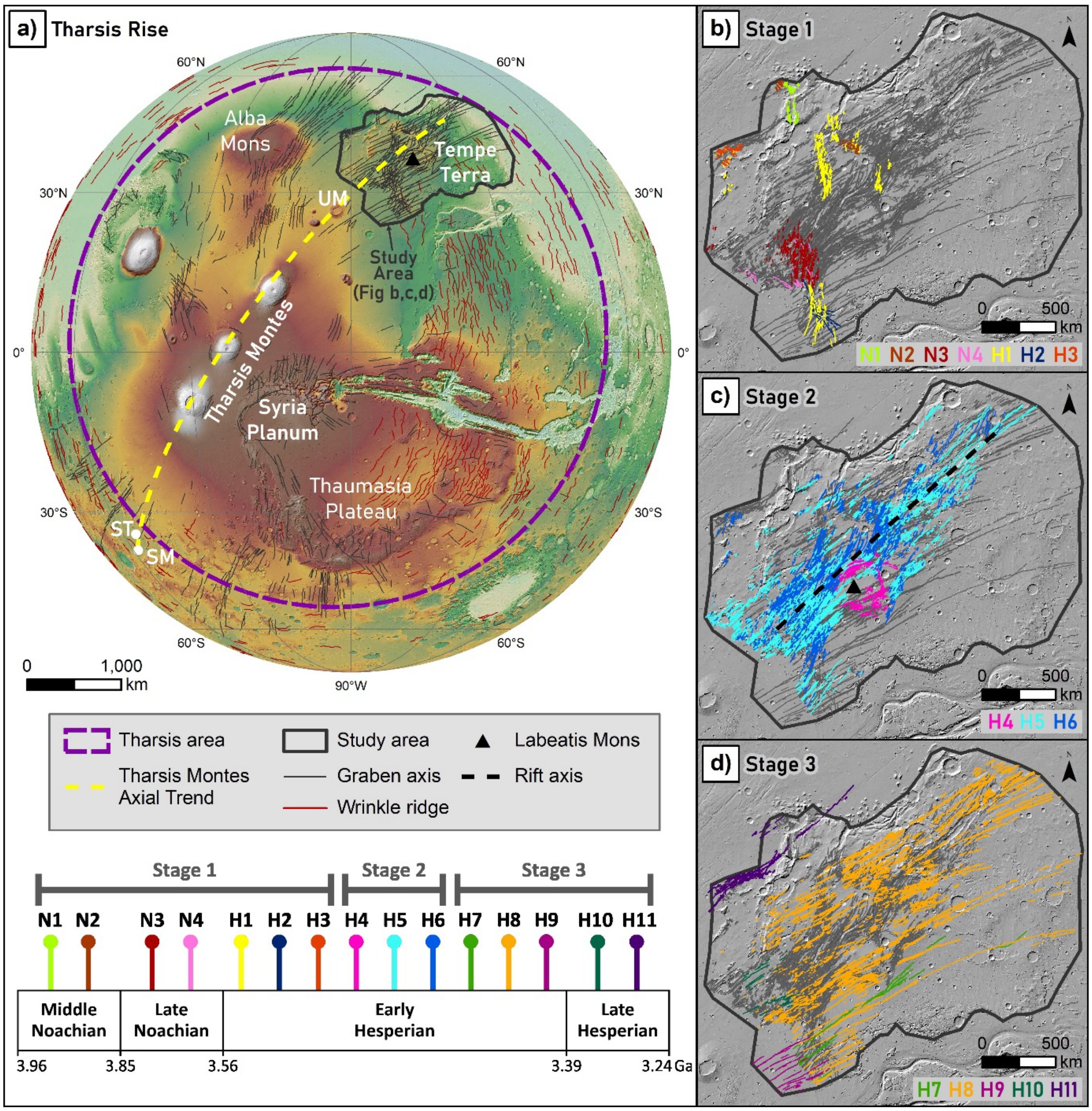

1.2 Assessing the origin of extensional surface structures on Mars

Given the lack of plate tectonics on Mars, we must look to other sources such as large-scale volcanism and/or magmatic activity, impact processes, and global contraction as major drivers of deformation (Banerdt et al., 1992). As a basis to assess the origin of the observed extensional structures in Tempe Terra, we compiled expected surface evidence of different proposed origins capable of graben formation on Mars (Table 1). Different origins of extension may produce either narrow graben systems (with faults that only penetrate the upper few kilometres of the crust) or rifting (with faults that potentially cut through the entire brittle lithosphere), both of which are observed in Tempe Terra (Hauber & Kronberg, 2001; Tanaka et al., 1991). However, as natural systems are inherently complex and heterogeneous, a clear-cut relationship between observable evidence and an interpreted source may be lacking. Even between volcanic and non-volcanic sources there is often non-unique evidence and solutions, such as radial fault patterns that can be associated with volcanic uplift, dyke intrusion, or flexural loading. This lack of clear evidence–source relationships makes it necessary to use a wide range of observations and evidence wherever possible, noting that not all listed evidence in Table 1 is required nor expected to be present.

In addition to sources for stress perturbations (i.e. differential stresses) in the crust, strain localisation is an important factor which can help initiate extension and allows for the formation of rift systems (Buck, 2007). This localisation may occur through magmatic intrusion and heating, pre-existing structures or zones of weakness, fault weakening (cohesion loss), and thermal advection due to stretching (Buck, 2007). Magmatic processes play a particularly important role in localising strain on volcanic planets by creating weak zones in the lithosphere, and these weak zones can interact with any form of stress generation (Corti et al., 2007; Grott et al., 2007; Hauber et al., 2010). Strain localisation within a fault population may be expressed in the spatial distribution of structures and their accumulated displacement, commonly in the form of large border faults and/or zones of intense faulting (Buck, 2007; Schultz et al., 2010). As such, deep seated origins that influence the rheological behaviour through crust and mantle may need to be considered (Table 1).

Based on our compilation of expected surface evidence (Table 1), it is necessary for rigorous assessment to characterize the following key features: surface patterns of faults in terms of orientation, degree of extension, and relationship to topography; graben morphology; large scale topography; crustal thickness variations; and spatial relationships of faults to volcanic and other non-tectonic surface features.

Table 1: Expected surface evidence of different sources of extensional stress causing graben formation on Mars. Evidence in bold is unique to one listed source. Local scale denotes sources which produce deformation and other effects in their immediate vicinity (<200 km), while regional scale indicates sources capable of producing far-field stresses and deformation several hundreds to thousands of km away. Literature in italics is related to general source and/or process evidence, others are specific to Mars. * indicates sources proposed for development of Tharsis Rise.

Source of Stress	Description	Scale	Evidence	Example Reference
VOLCANIC/ MAGMATIC				
Volcanic loading	Loading of lithosphere by adding material (i.e., volcanic extrusives) to the surface	Local	Circumferential pattern of arcuate and en echelon normal faults around the load	Golombek et al., 2009; Cailleau et al., 2003; Byrne et al., 2015
			Flexural trough or moat concentric to the load (between lower flanks of volcanic centre and circumferential faults)	Byrne et al.,2015
			Thicker crust at volcanic centre	Banerdt et al., 1992
			Stacked, convex terraces on volcano flanks	Byrne et al., 2015
Volcanic deflation/ core subsidence	Sinking of pre-existing volcanic centre through magma withdrawal or increasing density during cooling of magma	Local	Circumferential pattern of normal faults around volcanic centre	Mege & Masson, 1996; Tanaka & Davis, 1988; Cailleau et al., 2003
			Wristwatch pattern of graben when combined with regional extensional stress field	Cailleau et al., 2003
Volcanic uplift*	Uplift and bending of lithosphere from buoyancy forces above magma reservoirs at depth– includes mantle plumes	Regional or local	Radial pattern of normal faults around a volcanic centre	Carr, 1974; Mege & Masson, 1996; Cailleau et al., 2005
			Symmetric fault/fracture patterns which become less regular towards the centre of the dome	Carr, 1974; Cailleau et al., 2005
			Low density gravity anomaly under volcanic centre	Janle & Erkul, 1991; McGovern et al., 2001
			Dyke swarms centred on plume that diverge into two or three branches, or are radial to arcuate	Cailleau et al., 2003; Cailleau et al., 2005; Ernst et al., 2001; *Ernst et al., 1995*
			Hourglass pattern of graben when combined with regional extensional stress field	Cailleau et al., 2005; *Tibaldi et al., 2008*
			Topographic doming at the surface	*Allen & Allen, 2005*; Cailleau et al., 2005; *Crough, 1983*
Dyke intrusion	Vertical and/or lateral propagation of dykes from a magmatic centre through	Local	**Graben with uniform width, depth, length, and spacing across varied terrains and units (for grabens formed in a**	Tanaka et al., 1991

	rock due to magma driving pressure, creating tensile stress above		**single tectonic event)**	
			Radial or fan-like fault system geometry, extending far from volcanic source	Carr, 1974, Mege & Masson, 1996
			Graben aligned perpendicular to direction of minimum compressive stress	Cailleau et al., 2003
			Cross-sectional topographic signature with uplifted, convex graben flanks	Goudy & Schultz, 2005; Klimczak, 2014; Rubin & Pollard, 1988; Rubin, 1992; Schultz et al., 2004
			Spatial association with volcanic features (e.g. volcanic flows emanating from fissures in graben, linear vents)	Tanaka et al., 1991, Mege & Masson, 1996
			Linear surface features (pit crater chains, linear chasmata and U-shaped troughs)	Mege & Masson, 1996; Mege et al., 2003
			Large length of graben systems (individual graben or continuous linear trends of linked en echelon graben): 10s of km for smaller dyke swarms (e.g. from volcanic edifices), and >300km for larger swarms (from mantle plumes)	Mege & Masson, 1996; Ernst et al., 2001; *Ernst et al., 1995*
			Narrow, symmetrical and linear low relief ridges (dyke exposed at surface)	Mege, 1999
Magmatic underplating	The accumulation of mafic magmas in the lower crust and uppermost mantle around the Moho, where they achieve neutral buoyancy (no volcanic edifice required)	Local	Permanent topographic uplift without folding or thrusting	*Cox, 1993*
			Crustal thickening	*Cox, 1993*
			Flat Moho beneath a deep rift graben (i.e. lack of crustal thinning over rifted area) indicating magmatic compensation of crustal thinning	*Thybo & Nielson, 2009; Thybo & Artemieva, 2013*
NON-VOLCANIC				
Flexural loading*	Addition of material to the surface, causing downward displacement of the lithosphere	Regional	Radial compression (concentric wrinkle ridges) on the area with the load	Tanaka et al., 1991; Banerdt et al., 1992
			Circumferential extension (radial normal faults) in the area surrounding the load	Tanaka et al., 1991; Banerdt et al., 1992
			Topographic trough and low free-air gravity anomalies surrounding a load with high gravity	Phillips et al., 2001
Flexural uplift*	Buoyancy uplift of the lithosphere from locally thinning the crust and decreasing the density of the upper mantle, causing upward displacement (doming) of the lithosphere	Regional	Radial extension (concentric normal faults) on the uplifted area	Banerdt et al., 1992
			Circumferential compression (radial wrinkle ridges) in area surrounding the uplifted region	Banerdt et al., 1992

Isostatic compensation*	Support of topography by isostasy alone, from either complete relaxation of flexural stresses or zero net vertical displacement of the lithosphere	Regional	Circumferential extension (radial normal faults) on the elevated region	Tanaka et al., 1991; Banerdt et al., 1992
			Radial compression (concentric wrinkle ridges) in the area surrounding the elevated region	Tanaka et al., 1991; Banerdt et al., 1992
Horizontal gradients in gravitational potential energy (GPE) i.e., gravity spreading	Deviatoric stresses intrinsic to the lithosphere (rather than externally imposed) resulting from contrasts in gravity-driven potential energy between areas of thickened and/or elevated lithosphere (higher energy) and its surroundings (lower energy)	Regional or local	Extension (normal faults) over topographically high areas	Dimitrova et al., 2006; *Molnar & Lyon-Caen, 1988*
			Compression (thrust faults) on sloped flanks and topographically low areas	Dimitrova et al., 2006; Montgomery et al., 2009; *Molnar & Lyon-Caen, 1988*
			Normal faults and graben parallel to margins of extending area or chasm walls	Montgomery et al., 2009
			No rift flank uplift	*Allen & Allen, 2005*
Impact cratering	Stress from the impact of a meteoroid hitting a planet's surface in an instantaneous event	Regional or local	**Visible impact crater site (e.g. circular depression with elevated rim and ejecta blanket)**	*Kenkmann et al., 2014*
			Concentric and/or radial fractures and graben which decrease with distance from the impact site	*Jaumann et al., 2012*
			Massifs and ridges concentric to impact basin rim (for very large impacts)	Banerdt et al., 1992
			Impacts breccias containing clastic rock fragments and impact melt	*Kenkmann et al., 2014*; *Jaumann et al., 2012*
Aqueous fluid pressure	Elevated aqueous fluid pressures (generating non-igneous hydrofracturing) from impacts, freezing of groundwater, magma intrusion, liquefaction of water-saturated impact breccias during seismic activity etc.	Local	Mode I or hybrid fractures oriented perpendicular to least compressive stress	*Bons et al., 2022*; Tanaka et al., 1991
			Pit crater chains and troughs along graben	Tanaka et al., 1991
			Channels emanating from graben indicating significant volumes of discharged water	Tanaka et al., 1991
			Mineralised veins	*Bons et al., 2022*

2 Data and Methods

The goal of our analyses is to characterise the identified key features (section 1.2) in order to assess the evidence of different sources of faulting and distinguish between the options outlined in Table 1. All analyses are combined and presented based on the three tectonic stages in Tempe Terra (section 1.1; Orlov et al., 2022). Throughout this study, we use the term “local” to indicate effects isolated to Tempe Terra, and “regional” to indicate far-field effects extending beyond Tempe Terra – often across large parts of Tharsis.

Our analysis was conducted using the Tempe Terra fault dataset from Orlov (2022) and satellite imagery and topography from the Mars Reconnaissance Orbiter High Resolution Stereo Camera (HRSC), which has a typical image resolution of 12–25 m/pixel and digital elevation model (DEM) grid size of 75 m/pixel and 1 m height resolution within Tempe Terra (Jaumann et al., 2007; Neukum et al., 2004). Additional images were used from the Context Camera (CTX) which has a 6 m/pixel resolution (Malin et al., 2007). Topography data was also used from the Mars Orbiter Laser Altimeter (MOLA) and HRSC combined product (HRSC–MOLA DEM), which has a 200 m/pixel horizontal resolution and elevation accuracy of ±3 m (Fergason et al., 2018).

2.1 Analysis of fault geometries and graben morphology

In order to assess the likelihood of a volcanic or magmatic origin of faulting, we examined the spatial patterns of faults, their cross-sectional graben morphology, and their relationship to known regional and local features such as volcanic centres and regional tectonic trends. Using ESRI ArcGIS software, we traced geodesic paths for radial and circumferential patterns associated with each of the major Tharsis volcanoes (Tharsis Montes, Alba Mons, Olympus Mons) as well as the smaller volcanoes Labeatis Mons, Uranius Mons, Ceraunius Tholus, and Tharsis Tholus. We then compared these expected orientations to the position and alignment of fault sets from each tectonic stage. For radial patterns we consider both fanning relationships and subparallel patterns which converge on a common point (Ernst et al., 2001). This is a simplified approach and ignores the influence of interacting stress fields on otherwise potentially radial or circumferential stress patterns, such as those modelled for graben around Alba Mons (Cailleau et al., 2003; Cailleau et al., 2005).

We compared the spatial relationship of the faults from each stage to large regional patterns such as the Tharsis Montes Axial Trend and general radial orientation to the Tharsis Rise (which would require a broadly NE trend in Tempe Terra). We also digitised published stress trajectory maps from the Tharsis development models of Banerdt et al. (1992); Dimitrova et al. (2006); Mège and Masson (1996a, 1996b) and compared Tempe Terra faults to the predicted orientations and styles of faulting. We assessed the fit of six models which represent a variety of sources from Table 1, including: flexural loading, isostatic compensation, and flexural uplift (Banerdt et al., 1992); a Tharsis mantle plume (Mège & Masson, 1996a); detached crustal cap, which combines loading and isostasy models (Tanaka et al., 1991); and gradients of gravitational potential energy (GPE; Dimitrova et al., 2006). Spatial relations of faults to volcanic or non-volcanic surface features such as small vents, pit crater chains, channels, flows, and canyons were also considered.

Using the HRSC–MOLA DEM we looked for areas of high or low topography in relation to faulted regions for each stage, in order to identify features such as domes or flexural troughs. We also took a series of topographic profiles from the HRSC DEMs across representative graben from the different tectonic stages to determine the typical cross-sectional graben shape of each stage. A flat or concave up (ski ramp) shape to the graben flanks is expected for a standard, 'tectonic' graben while convex graben flanks are an indicator of the presence of a dyke (Goudy & Schultz, 2005; Rubin, 1992; Rubin & Pollard, 1988; Schultz et al., 2004). Some areas were difficult to assess with this method due to dense faulting with a lack of free space on the graben flanks, and variability in DEM quality in comparison to graben width. Our assessment of topographic patterns more generally is complicated by later volcanic cover and/or the effects of erosion.

2.2 Extension analysis: Quantification and spatial variation

To visualise spatial variations in extensional strain across Tempe Terra, we produced a series of extension profiles for all fault sets and combined these for each tectonic stage. We extracted topographic profiles spaced 100 km apart and aligned perpendicular to the average strike of each fault set. We measured the vertical displacement (d) of each fault along a profile and converted this to heave (e) using the approach of Golombek et al. (1996):

$$e = \frac{d}{\tan \alpha}$$

We assumed a consistent dip (α) of 60° for all faults, and while this necessary simplification is typical for studies of Martian extensional faults, it introduces error into the calculation (Golombek et al., 1996). Total extension across each profile is taken as the sum of the heaves of all intersected faults. We favour total extension as calculations of strain (which divide the total extension by a reference length) are highly dependent on the chosen length of a reference profile and are therefore difficult to compare between published works. Nevertheless, sources of error persist in defining the amount of total crustal extension. Data resolution may fall below the threshold needed to image narrow graben and has inherent uncertainty in vertical accuracy, while environmental considerations such as erosion of the footwall and graben infill may reduce the observable surface displacement

(Golombek et al., 1996; Ziegler & Cloetingh, 2004). Measurements of vertical offset used in our calculations are therefore considered a minimum.

To visualise spatial variations in strain accommodation between faults from the same temporal stage, we gridded our measurements of individual fault heave into 2D heat maps. For each tectonic stage we used inverse distance weighted (IDW) interpolation in ArcGIS to convert our point measurements of fault heave into continuous rasters coloured by magnitude. IDW is a simple and efficient interpolation method but is sensitive to data outliers (Wu & Hung, 2016) and the heave parameter itself has the same limitations as the extension calculation. A detailed description of the gridding method, including parameters, can be found in Supporting Information.

2.3 Fault reactivation: Slip and dilation tendency

Fault reactivation is a common complicating factor when attempting to interpret the origin of faults so it is helpful to understand when and where it is likely to have occurred. Slip and dilation tendency analysis (Ferrill et al., 1999; Morris et al., 1996) can be used to quantify and visualise the likelihood of fault reactivation: where faults have a high tendency for slip and/or dilation in a given stress field, they are considered likely locations for reactivation (Morris et al., 1996; Worum et al., 2004). Physically, slip tendency describes the likelihood of shear failure resulting in the accumulation of additional displacement through dip-slip motion along the fault plane, while dilation tendency describes the likelihood of tensile failure resulting in horizontal motion (Ferrill et al., 2020). We use exact rather than normalised values for slip and dilation tendency. Faults are considered to be ideally oriented for slip when they have a slip tendency (T_s) ≥ 0.6 (Ferrill et al., 1999). In our analysis we describe faults as being optimally oriented for slip ($T_s \geq 0.6$), well oriented for slip ($0.5 < T_s < 0.6$), moderately oriented for slip ($0.3 < T_s < 0.5$), or poorly oriented for slip ($T_s < 0.3$). We define the dilation tendency (T_d) of faults as high ($T_d > 0.6$), moderate ($0.4 < T_d < 0.6$), and low ($T_d < 0.4$).

We created maps of slip and dilation tendency to examine the extent of likely fault reactivation during Tempe Terra's structural evolution. Our approach involved a geometrical analysis of fault orientations within a series of simple Andersonian stress fields where σ_1 is vertical, σ_2 is parallel to the average fault strike and 66% of σ_1, and σ_3 is perpendicular to the average fault strike and 32% of σ_1. We made no assumptions about the local magnitudes of stress active in Tempe Terra as only the ratio of stress matters in this approach (Worum et al., 2004). For this analysis we examined the effects of stress fields representing Stage 2 (σ_3 azimuth 117°) and Stage 3 (σ_3 azimuth 150°) activity on Stage 1 and Stage 2 faults. We could not assess reactivation of Stage 3 faults as we lack indicators of major Amazonian activity within Tempe Terra on which to base stress fields after Stage 3. To remain consistent with our approach for extension, we used an assumed dip of 60° for all faults. The reliability of the results depends on the validity of our input stress fields, as well as uncertainty regarding the fault dip. A detailed description of the analysis method can be found in Supporting Information.

2.4 Gravity and crustal thickness

Variations in thickness and gravity response of the Martian crust provide evidence for several potential sources of stress (Table 1). We therefore include qualitative observations of local gravity anomalies and crustal thickness within Tempe Terra from the Goddard Mars Model–3 (GMM-3) Bouguer gravity and derived crustal thickness models (Genova et al., 2016). GMM-3 utilises gravity data from the Mars Global Surveyor, Mars Odyssey, and Mars Reconnaissance Orbiter and has a global surface resolution of ~115 km, although this can vary with latitude and other factors (Genova et al., 2016). The Bouguer anomaly map of Genova et al. (2016) was calculated assuming a bulk density for the crust of 2900 kg/m^3 and removing the effects of the hemispheric dichotomy and polar flattening. Their map of crustal thickness was derived from a nonlinear inversion for relief on the crust-mantle boundary, assuming a mantle density of 3500 kg/m^3 (Genova et al., 2016).

It is important to keep in mind that what we can observe in these datasets is the current state of the Martian crust, which is the combined result of Tempe Terra's geologic and tectonic history. It is therefore challenging to separate the effects of different stages of activity on the gravity response or crustal thickness, or assign ages to the various observed features.

3 Results and Analysis

3.1 Geometrical and extensional characteristics

3.1.1 Stage 1 (Middle Noachian – Early Hesperian)

Fault patterns, geometries and relationships to regional trends: The N–S faults which make up the bulk of Stage 1 (82% of faults) do not have a radial or circumferential relationship to any Tharsis volcanoes or to the Tharsis Rise as a whole and are instead aligned tangentially to Tharsis. Stage 1 is the most poorly aligned to Tharsis stress trajectory models, and while most models predict extension over Stage 1 faults, the orientation of the stresses is a poor fit for the observed structures (Table 2; Figure 2a, blue arrows). The patches of NW-oriented faults which are dispersed across western Tempe Terra align partially with circumferential trends around the Tharsis Montes, Uranius Mons and Tharsis Tholus volcanoes, as well as the Tharsis Rise generally, but they do not form a continuous system. Neither the orientation nor location of Stage 1 faults are aligned with the Tharsis Montes Axial Trend. The primary N–S trend is approximately perpendicular to the highland–lowland dichotomy boundary, regardless if that is drawn along the north edge of Tempe Terra (Wilhelms & Squyres, 1984) or farther to the south of Tharsis (Andrews-Hanna et al., 2008).

The N–S structures are also parallel with the large, linear canyons of Tanais Fossae (Figure 2b). This canyon system occupies an exposed Middle Noachian unit that lacks Noachian faults but is surrounded by Stage 1 structures (Figure 2a, purple outline). This canyon system has been heavily eroded (Figure 2b), and other structures in the same north-western part of Tempe Terra, such as the large Quepem Fossa graben (Figure 2a), also have a degraded appearance compared to faults further south. At the central western edge of Tempe Terra there is a system of narrow, symmetrical, linear ridges that trend mostly N and NW and sometimes intersect to form branching networks (Figure 2c). The ridges occur only on blocks of Late Noachian terrain that are exposed above younger lava flows and are cut by faults from Stage 1 and Stage 2 (Figure 2c). They are associated with the graben of Stage 1 both spatially and in orientation. While not located in close proximity to the faults, a volcano edifice at 70° W, 44.5° E (UV2 on Figure 2a) is a volcanic surface feature similar in age to Stage 1 tectonic activity. UV2 is the only exposed Early Noachian unit in Tempe Terra (Figure 2a, red outline; Tanaka et al., 2014) and appears morphologically similar to Tyrrhenus Mons (formally Tyrrhena Patera) in the southern highlands near the Hellas impact basin.

Faults tend to occur in topographically high regions which have not been buried by later lava flows. There is an area of locally high topography that links faults from the south of Tempe Terra to the northern edge of the platea (Figure 2a), including the Tanais Fossae canyon system. Despite the impact of post-tectonic modification and erosion, the largest graben and canyon systems are in the areas of highest topography. We clearly have an incomplete record of structures from this period in the west of Tempe Terra (Figure 2a, purple outline and surrounds), but we lack any structures of comparable age or orientation in the eastern half of the plateau.

Graben topographic profiles typically have flat or concave flanks (Figure 3a), while convex flank uplift is rare. Other graben dimensions (length, width, depth) are not uniform across Tempe Terra, with regions of long, narrow graben in the south (<1 km wide) contrasted with shorter, en echelon graben in Ascuris Planum (1–3 km wide), and a ~25 km wide, rift-style graben at Quepem Fossa.

Graben extension and heave: Total extension across Stage 1 faults is variable but generally higher in the north of Tempe Terra (Figure 2d). Extension ranges from 0.2 km to 9.2 km, which is the lowest of all the stages. However, it is important to note that this stage also has the smallest number of faults and many Noachian structures have likely been buried or modified, so we are not seeing the full picture and these strain estimates are minima. The heave map shows that extension has not been accommodated uniformly across the faults (Figure 2e), with individual values ranging from 6 m to

3528 m and a median of 103 m per fault. There is localisation of heave onto a few large faults making up Quepem Fossa, with the rest of the faulted region displaying a more even distribution of heave between the smaller graben (Figure 2e). While there is a relatively large amount of extension where heave is localised, the greatest total extension is in areas where there is a high density of smaller-offset faults with evenly distributed heave.

Table 2: Fit of Tempe Terra tectonic patterns to Tharsis stress trajectory models. Predictions from models of stress from the development of Tharsis are compared to structures from each tectonic stage and assessed for fit. Red indicates no fit, orange partial fit, and green good fit.

Tharsis Model		**Model Prediction in Tempe Terra**	**Fit to Stage 1 structures**	**Fit to Stage 2 structures**	**Fit to Stage 3 structures**
Flexural loading[1]	Strain type	Extension in east two thirds; shortening in west third	No	*Partial* (Figure 4a)	*Partial*
	Structure orientation	Faults radial to Tharsis; oriented ~50–65°	No	*Partly aligned to rift axis only* (Figure 4a)	**Yes**
Isostatic compensation[1]	Strain type	Extension in west two thirds; shortening in east third	**Yes** (Figure 2a)	*Partial*	*Partial*
	Structure orientation	Faults radial to Tharsis; oriented ~50–70°	No (Figure 2a)	*Partly aligned to rift axis only*	**Yes**
Flexural uplift[1]	Strain type	Extension	**Yes**	**Yes**	**Yes**
	Structure orientation	Faults concentric to Tharsis; oriented ~120–135°	*Aligned to NW faults only*	No	No
Detached crustal cap[2]	Strain type	Extension	**Yes**	**Yes**	**Yes**
	Structure orientation	Faults radial to Tharsis; oriented ~50–70°	No	*Partly aligned to rift axis only*	**Yes**
Plume[3]	Strain type	Extension	**Yes**	**Yes**	**Yes** (Figure 5a)
	Structure orientation	Faults radial to Tharsis; oriented ~50–70°	No	*Partly aligned to rift axis only*	**Yes** (Figure 5a)
Gravitational potential energy (GPE)[4]	Strain type	Normal & oblique extension in west half; oblique shortening in east half	**Yes**	*Partial*	No
	Structure orientation	Faults radial to Tharsis; oriented ~50–70°	No	*Partly aligned to rift axis only*	**Yes**

[1]Banerdt et al. (1992), [2]Tanaka et al. (1991) with crustal cap outline from Mège and Masson (1996b), [3]Mège and Masson (1996a), [4]Dimitrova et al. (2006)

Figure 2: Stage 1 tectonic patterns and associated observations. **a)** Extent of Stage 1 faults with overlay of predicted stress type and orientation from isostatic compensation model of (Banerdt et al., 1992). UV2 = unnamed volcanic centre. Background is colourised terrain from the HRSC–MOLA DEM. **b)** Tanais Fossae canyon system. **c)** Branching systems of narrow linear ridges shown on CTX image. **d)** Total extension across Stage 1, coloured by magnitude. **e)** Heat map of individual fault heave.

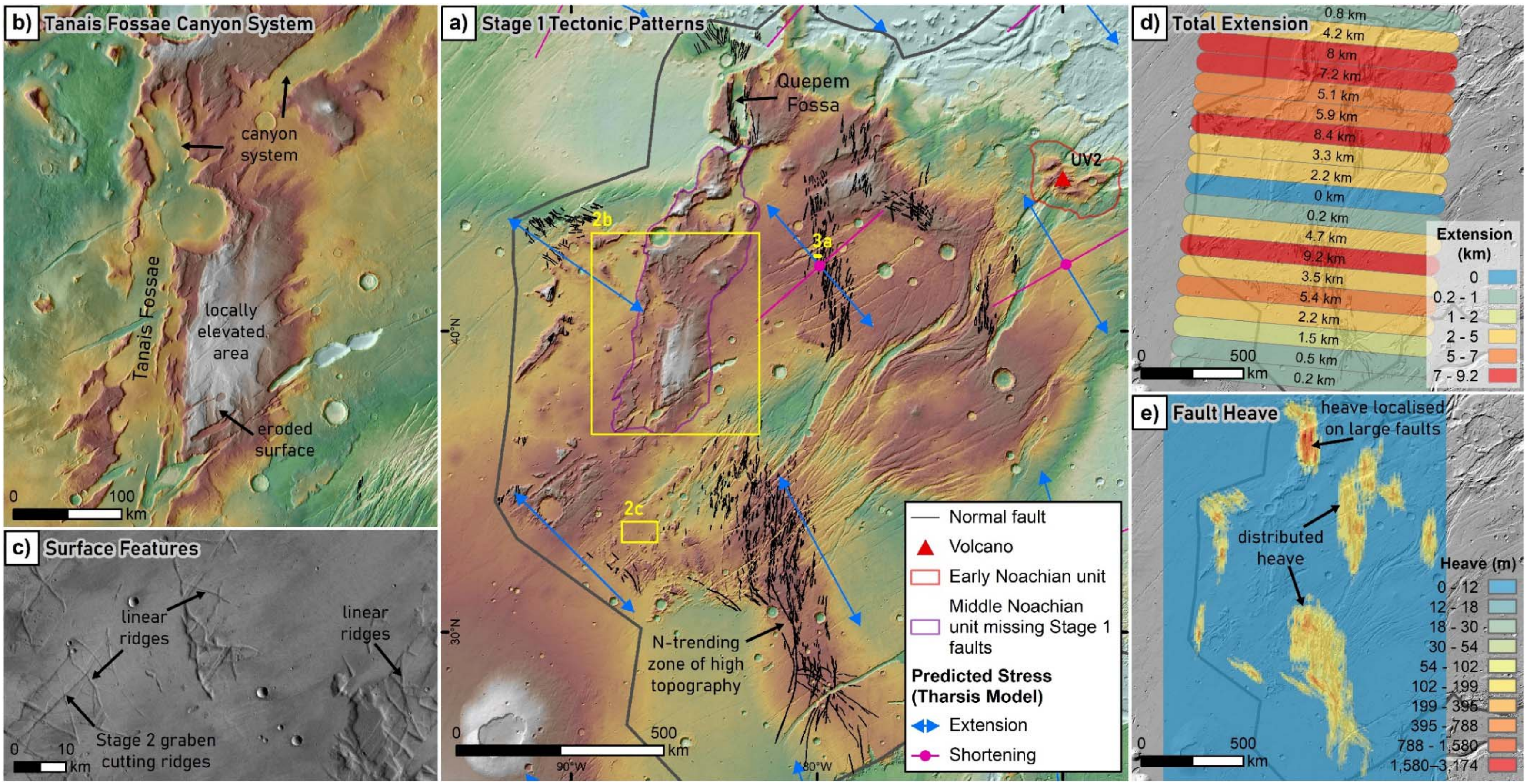

Figure 3: Representative graben profiles for each tectonic stage. **a)** Profile of Stage 1 graben with flat and concave flanks, location shown on Figure 2a. **b)** Profile of Stage 2 graben with flat flanks, location shown on Figure 4a. **c)** Profile of Stage 3 graben with convex flanks, location shown on Figure 5a. All profiles from HRSC DEM. Note that horizontal scale is consistent but vertical scale changes for each subfigure.

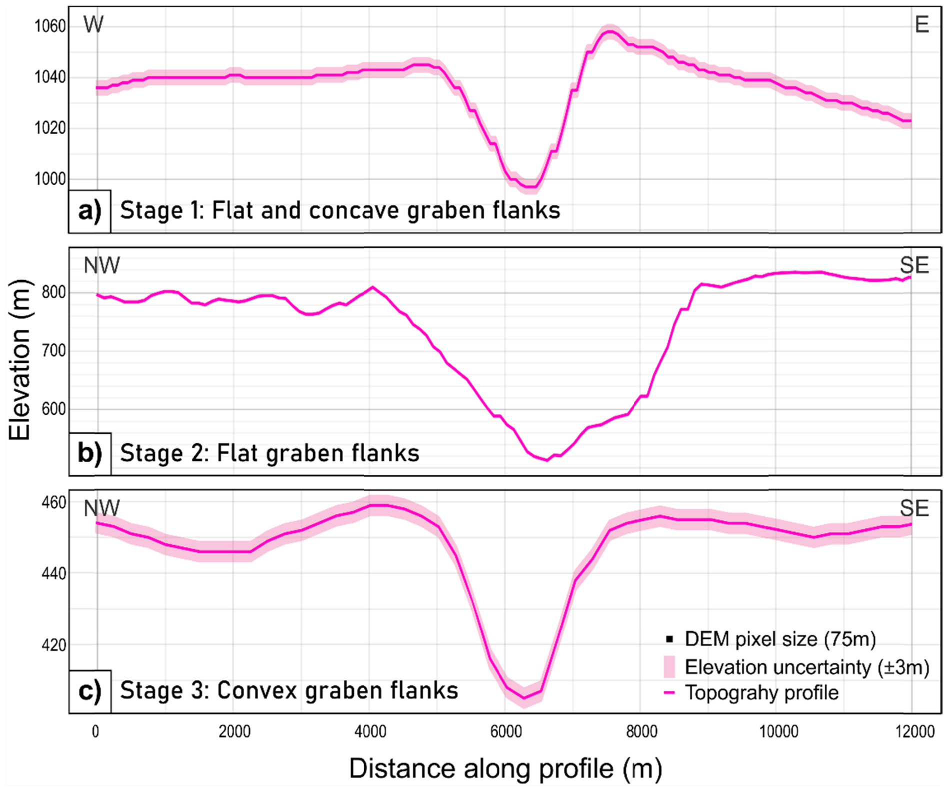

3.1.2 Stage 2 (Early Hesperian)

Fault patterns, geometries and relationships to regional trends: Faults of Stage 2 have strong spatial relationships to the Tharsis Rise, being both broadly radial to a region south of the Tharsis Montes on the topographic bulge and aligned with the Tharsis Montes Axial Trend. The axis of the Tempe Rift and region of highest spatial density of faulting occur along the line of the Tharsis Montes Axial Trend (Figure 4a, white dashed line), with both rift-parallel faults and rift-oblique faults only having minimal occurrence outside this area. Several Tharsis stress models predict extension in the areas covered by Stage 2 faults, but align only with rift-parallel faults and not rift-oblique faults (Figure 4a, blue arrows; Table 2). The faults lack any fanning pattern but if we consider subparallel patterns that radiate from a common point, then rift-oblique faults are radial to Syria Planum (Figure 4a, purple arrow) and partially radial to Tharsis Tholus, and rift-parallel faults are radial to the Tharsis Montes. There is also an arcuate pattern of faults circumferential to Labeatis Mons which forms a wristwatch pattern in combination with the Tempe Rift (Figure 4b).

There is clear evidence of volcanic surface features associated with Stage 2, with three intra-rift volcanoes: Labeatis Mons and two unnamed volcanic centres (UV1 and UV2; Figure 4a). Labeatis Mons and UV1 have impacted the shape of the rift, with the main rift graben being deflected around Labeatis Mons (Figure 4b) and an hourglass pattern centred on UV1 formed to the southeast of the main rift axis (Figure 4a, b). UV2 sits across the main rift graben at the NE end of the rift and has been highly modified by Stage 2 faulting (Figure 4c). All three volcanoes have locally elevated topography representing the volcanic edifice. Pit crater chains are a minor feature associated with graben from this stage, with a few occurring in the western half of Tempe Terra, but the majority are aligned with Stage 3 structures. Aligned with a narrow graben on the eastern side of the main rift is an oval-shaped collapse depression and associated NE-trending narrow, linear ridges (Figure 4d), which are similar to those described for Stage 1 but are fewer in number and lack branching intersections.

Across Tempe Terra, the topography shows an overall decline in elevation from SW to NE (Figure 4a, black arrow). Where faulting is concentrated, there is a broadly uplifted region around Labeatis Mons as well as at the SW end of the rift. There is also a region of lower elevation directly around the Labeatis Mons edifice, forming a semi-circular trough that is most pronounced on the northern side (Figure 4b). This trough is surrounded by a ring of higher elevation where the majority of circumferential faults appear (Figure 4b).

Graben profiles are variable in morphology but most commonly have flat or concave flanks (Figure 3b). The graben typically occur in zones of numerous, closely-spaced, cross-cutting faults, rather than as long continuous trends such as in Tantalus Fossae at Alba Mons. Graben dimensions are variable across the region and there is a distinct separation between the narrow graben (1–3 km wide) that make up the majority of structures, and the large rift graben which are significantly longer, wider (>15 km), and deeper (Figure 4b).

Graben extension and heave: The pattern of total extension across Stage 2 faults shows a clear increase from NE to SW, i.e., with increasing proximity to Tharsis (Figure 4e, black arrow). Extension ranges from 1.1 km to 45.4 km, which is the highest of all stages and reflects that faulting from this stage accounts for over half the total cumulative fault length in Tempe Terra (Orlov et al., 2022). Extension measurements along the western edge of the plateau are affected by Late Hesperian lava flow cover, with faults only preserved on remaining high blocks. As with Stage 1, the heave map shows the extension has not been accommodated uniformly across the faults, with localisation of heave onto large border faults along the central axis of the Tempe Rift (Figure 4f). Individual fault heaves range from 3 m to 7040 m, with a median of 169 m per fault. Along the rift axis there is a change from high heave localised on a few faults in the NE to lower heave evenly distributed across a wider zone of high density faults in the SW, closer to Tharsis (Figure 4f). This change mirrors the increase in extension, with the greatest total extension accommodated where there is evenly distributed heave across many faults.

3.1.3 Stage 3 (Early – Late Hesperian)

Fault patterns, geometries and relationships to regional trends: Stage 3 faults are broadly radial to a region just north of the Tharsis Montes on the Tharsis Rise, and generally align most closely of all the Tempe Terra stages to the various proposed Tharsis stress models (Table 2). The Tharsis plume model (Figure 5a; Mège & Masson, 1996a) and detached crustal cap model (Tanaka et al., 1991) best match the style and orientation of faults from this stage, but the flexural loading and isostasy models (Banerdt et al., 1992) also have partial fits (Table 2). The fault orientations have no strong radial or circumferential relationship to any specific Tharsis volcanoes, and are not aligned with or concentrated along the Tharsis Montes Axial Trend. The youngest fault sets from this stage, which are found on the western edge of the plateau (Figure 1d, sets H9, H10, H11), continue outside of the study area towards the centre of Tharsis, and in the north join the Tantalus Fossae graben system around Alba Mons (Figure 5a).

There are over 100 linear surface features of various morphologies aligned with Stage 3 faults across Tempe Terra. Almost all pit crater chains in Tempe Terra are associated with graben from this stage or follow the same ENE trend (Figure 5b). Linear chasmata and U-shaped troughs (as described by Mège et al., 2003) are common, particularly in Ascuris Planum and the west of the plateau, and are aligned with or directly continue from graben (Figure 5c). Small volcanic features such as lines of vents, fissures and low shields (Figure 5d) are also aligned with faults at the western edge of Tempe Terra (Moore, 2001). At the southern edge of the plateau, the Labeatis Fossae flood canyon feature and many of its associated linear cracks are parallel to sub-parallel with the graben orientation (Figure 5a).

Graben cut across the full width of Tempe Terra and the full range of plateau topography in continuous linear trends (Figure 5a). The pattern of faults is not concentrated along or uniquely associated with areas of high or low topography. Profiles of the graben themselves commonly show convex flank uplift in the ~2–4 km surrounding the border faults (Figure 3c). Rather than the zones of crosscutting graben seen in Stage 2, we see long, continuous trends formed by the alignment of many graben with typically uniform dimensions (Figure 5a). While graben along strike from each other tend to be consistent, across Tempe Terra there is some variation in width, from very narrow

(<1 km wide) in the south, to more typical dimensions for Tempe Terra (1–3 km wide), to graben around Labeatis Mons and the northeast of the plateau that are slightly wider (3–6 km wide).

Graben extension and heave: Total extension across Stage 3 faults generally increases towards the centre of Tempe Terra, peaking just west of the Labeatis Mons volcanic centre (Figure 5e, black arrow). Extension ranges from 1.1 km to 24.2 km, placing it in the middle of the range of extension across the three stages. As with Stage 1 and Stage 2, total extension measurements are affected by overlying lava flows at the western edge of the plateau (Figure 5a, purple area). Earlier fault sets from this stage are buried by volcanic units that were then cut through by more recent fault sets (Figure 5a; Orlov et al., 2022). The heave map shows extension has been accommodated in a more uniform way between faults (Figure 5f). Individual fault heaves are from 3 m to 2228 m, with a median of 119 m, which is the smallest range of all the stages. This is also reflected spatially, with an even distribution of heave between faults spread all across Tempe Terra.

Figure 4: Stage 2 tectonic patterns and associated observations. **a)** Extent of Stage 2 faults with overlay of predicted stress type and orientation from flexural loading model of Banerdt et al. (1992). See Figure 2a for legend. White dashed line is Tharsis Montes Axial Trend. LM = Labeatis Mons, UM = Uranius Mons, UV1 and UV2 = unnamed volcanic centres. Background is colourised terrain from the HRSC–MOLA DEM. **b)** Labeatis Mons volcano showing associated circumferential faults and topographic low surrounding central edifice. Inset shows schematic of hourglass and wristwatch fault patterns. **c)** Unnamed volcanic centre at north-eastern end of rift, showing local elevation and eroded morphology. **d)** Collapse depression and linear ridges along same trend as rift, shown on CTX image. **e)** Total extension across Stage 2, coloured by magnitude. **f)** Heat map of individual fault heave.

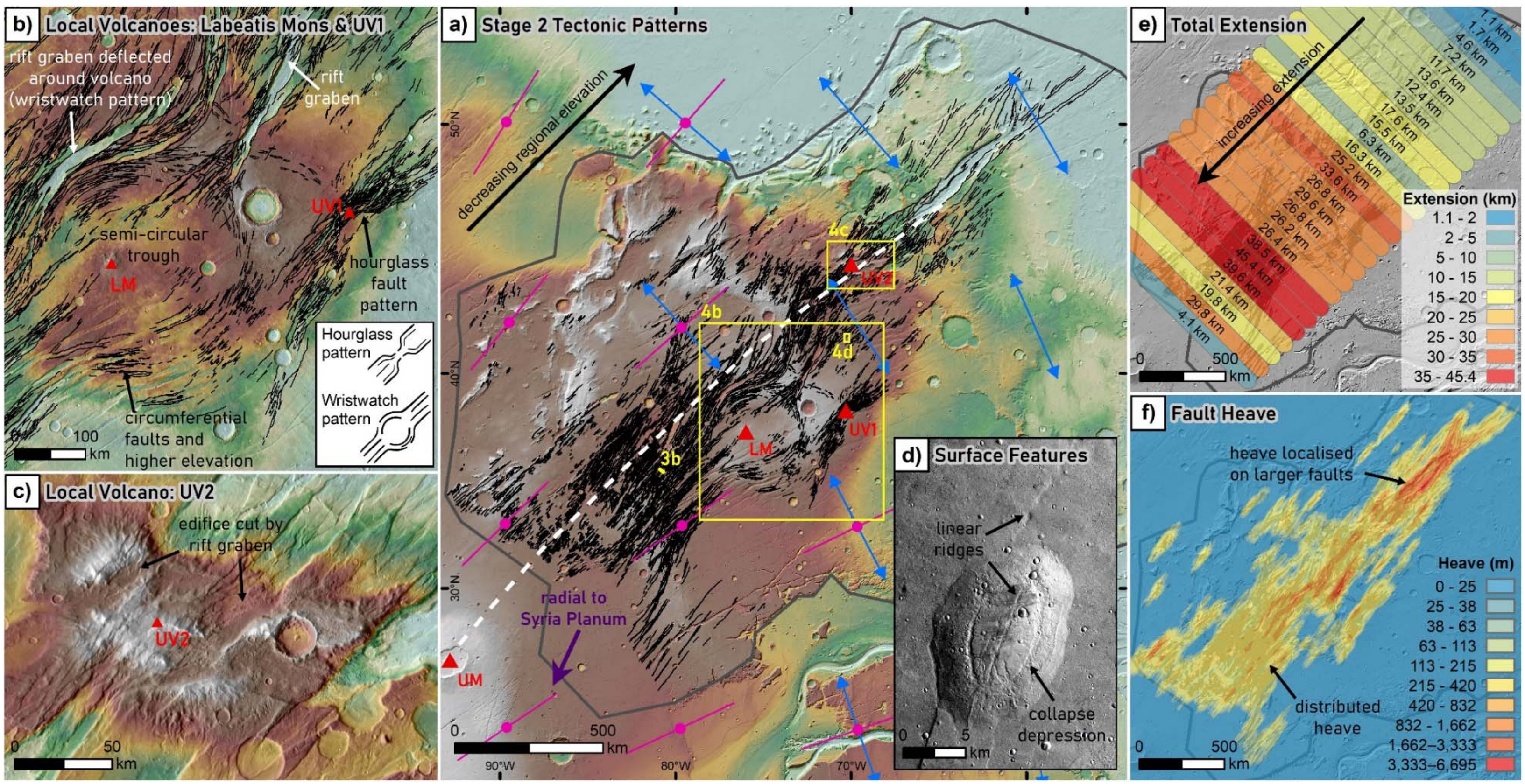

Figure 5: Stage 3 tectonic patterns and associated observations. **a)** Extent of Stage 3 faults with overlay of predicted stress orientation from Late Hesperian–Amazonian plume model of Mège and Masson (1996a). Background is colourised terrain from the HRSC–MOLA DEM. **b)** Pit crater chain along centre of graben cutting across earlier, Stage 2 rift-related faults. **c)** Linear chasmata along ENE trend of Stage 3 graben in Ascuris Planum. **d)** Small shield volcanoes with visible central vents. **e)** Total extension across Stage 3, coloured by magnitude. **f)** Heat map of individual fault heave.

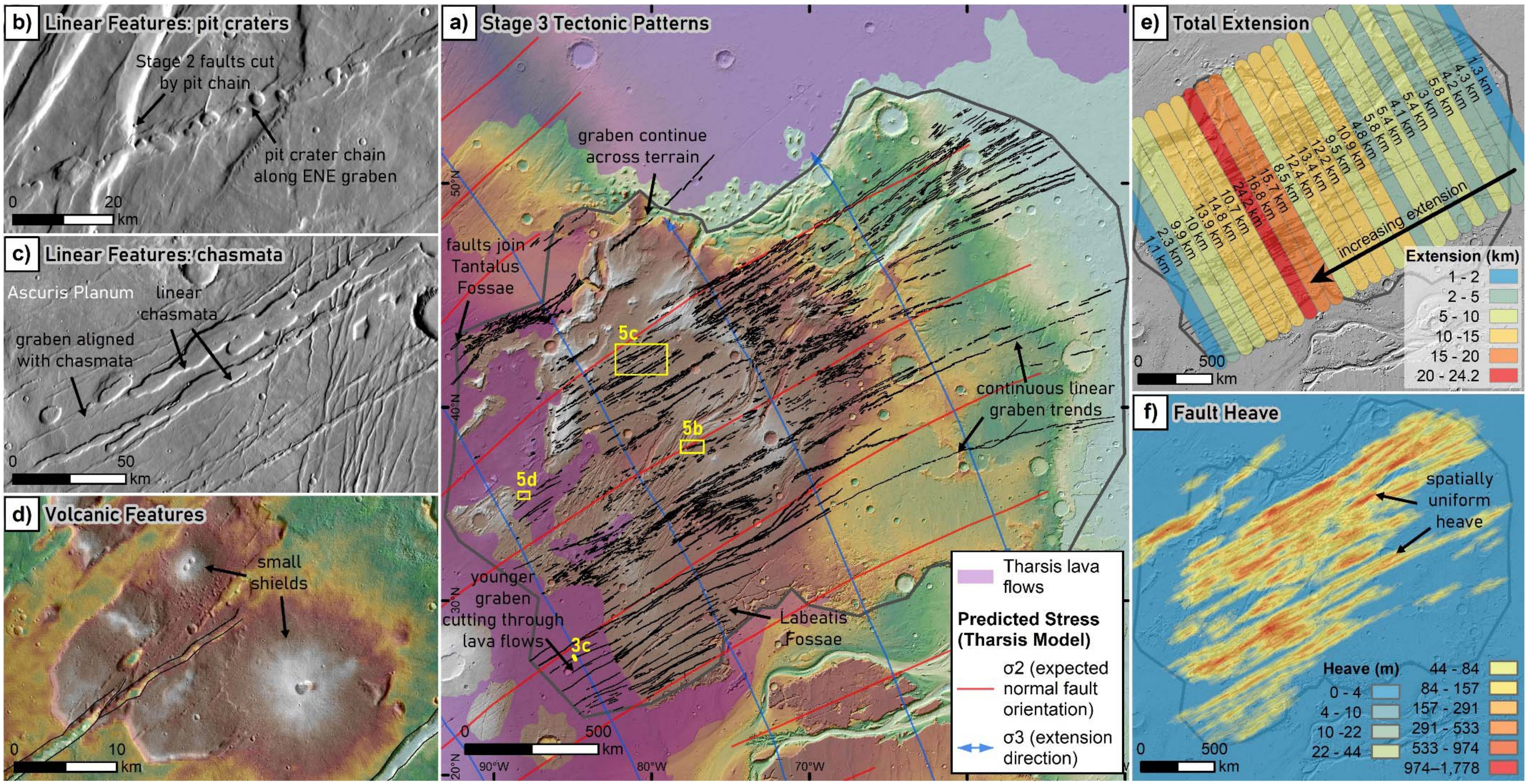

3.2 Patterns of fault reactivation

Stage 1 fault reactivation during Stage 2: For Stage 1 faults under the Stage 2 stress field (σ_3 oriented 117°), slip and dilation tendency is highest on N-trending faults and lowest for NW-trending faults (Figure 6a, b). Most N-trending faults are optimally or well oriented for slip in the Stage 2 stress field, with high average slip tendency (0.54) and dilation tendency (0.69), so have a high possibility of reactivation during Stage 2. NW-trending faults are generally poorly oriented for slip, with low average slip tendency (0.28) and moderate dilatation tendency (0.44), so are less likely to have been reactivated during Stage 2. In all scenarios, there is commonly significant along-strike variations in slip and dilation tendency for a single fault due to corrugations in the fault trace or changes in orientation (Figure 6, insets).

Stage 1 and 2 fault reactivation during Stage 3: Under the Stage 3 stress field (σ_3 oriented 150°), Stage 1 faults have lower overall slip and dilation tendency than in the Stage 2 stress field, with the highest values on the few WNW-trending faults and lowest values for NNW-trending faults (Figure 6c, d). N-trending faults are generally moderately oriented for slip, with moderate average slip tendency (0.37) and moderate dilatation tendency (0.51), so are unlikely to have been extensively reactivated during Stage 3. NW-trending faults range from moderately to poorly orientated for slip, with low average slip tendency (0.31) and moderate dilatation tendency (0.46), which is higher than in Stage 2 but still represents a low likelihood of reactivation during Stage 3.

For Stage 2 faults, slip and dilation tendency is highest in rift-axis-parallel faults (average strike 45°) and lowest for faults in the N-trending, sigmoidal section of the rift (Figure 6e, f, inset). Rift-parallel faults, including the majority of the large rift border faults, are optimally or well oriented for slip and dilation, while rift-oblique faults are only moderately well oriented. The circumferential faults around Labeatis Mons vary with strike, from well-oriented for slip and dilation when rift-parallel, to poorly oriented when rift-perpendicular (Figure 6e, f). Overall, Stage 2 faults have a high average slip tendency (0.50) and dilatation tendency (0.63), so there is a high possibility of reactivation of many of these faults during Stage 3.

Figure 6: Assessment of fault reactivation potential under different stress regimes, for 60° fault dip scenario. Colours show slip and dilation tendency, see legends in a) and b). Insets show zoom illustrating along-fault variation. Background is shaded relief HRSC–MOLA DEM. **a)** Slip tendency of Stage 1 faults under Stage 2 stress field (σ_3 oriented 117°). **b)** Dilation tendency of Stage 1 faults under Stage 2 stress field. **c)** Slip tendency of Stage 1 faults under Stage 3 stress field (σ_3 oriented 150°). **d)** Dilation tendency of Stage 1 faults under Stage 3 stress field. e**)** Slip tendency of Stage 2 faults under Stage 3 stress field (σ_3 oriented 150°). **f)** Dilation tendency of Stage 2 faults under Stage 3 stress field.

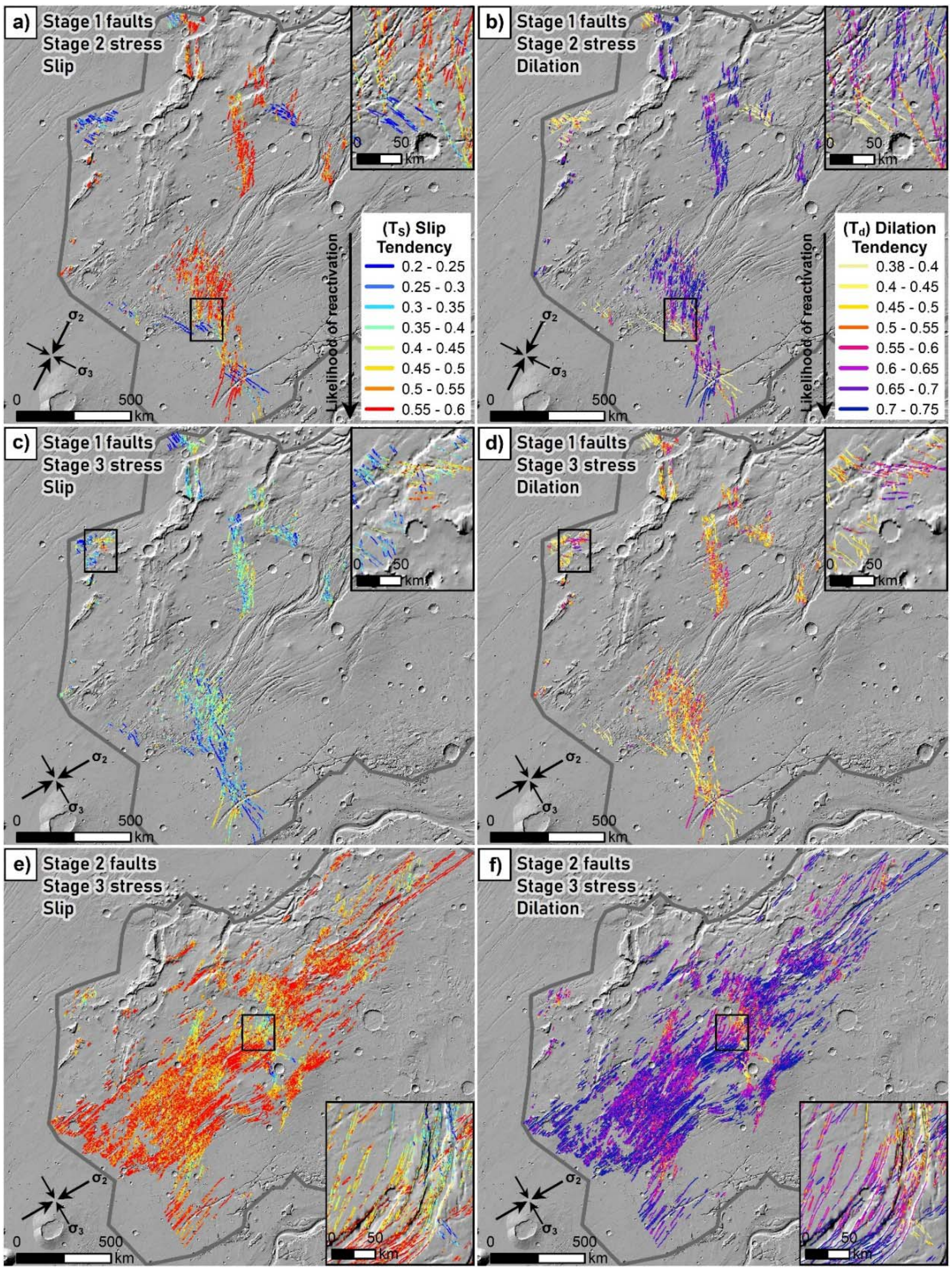

3.3 Local crustal thickness and density variations

Gravity within Tempe Terra ranges from -329 to 78 mGal. A large negative Bouguer anomaly (-329 mGal) lies over central Tempe Terra and is the dominant feature of the local gravity response (Figure 7a). All of the volcano edifices within Tempe Terra are located within this broad anomaly, but are not associated with any additional smaller anomalies (Figure 7a). The negative gravity response indicates either lower density near-surface crustal material and/or a deeper crust-mantle transition and therefore thicker crust. This feature is one of three substantial negative Bouguer anomalies within Tharsis, the others being over Alba Mons (-488 mGal) and around Arsia Mons and the Thaumasia Highlands (-426 mGal).

Crustal thickness ranges from 36.7 to 65.6 km across the study area (Figure 7b, white outline). This nearly 30 km variation reflects the contrast between the Tempe Terra plateau and parts of the northern lowlands captured at the northern and eastern edges of the study area. The crust is thickest in central and northern Tempe Terra, largely corresponding to the regions of lowest gravity (Figure 7). There is also a ring of thick crust surrounding Labeatis Mons (Figure 7b), which correlates with the location of circumferential faults which surround the volcano. We do not see any thinning of the crust under the large graben of the Tempe Rift from Stage 2, nor under Quepem Fossa and the Tanais Fossae canyon system from Stage 1, and in some places the crust is actually thickened under these highly extended areas (Figure 7b). We also see no clear relationship between crustal thickness and the changing style of the Tempe Rift from a single deep graben in the NE to a wide zone of distributed faulting the SW (Figure 7b).

Figure 7: Local Bouguer anomaly and crustal thickness within Tempe Tera. White outline is study area. Red triangles are volcanoes: LM = Labeatis Mons, UM = Uranius Mons, UV1 and UV2 = unnamed volcanic centres. Background is shaded relief HRSC–MOLA DEM. A) Bouguer anomaly map of Tempe Terra in mGal. B) Crustal thickness map of Tempe Terra in km. Colourbar is stretched to thickness range within study area only.

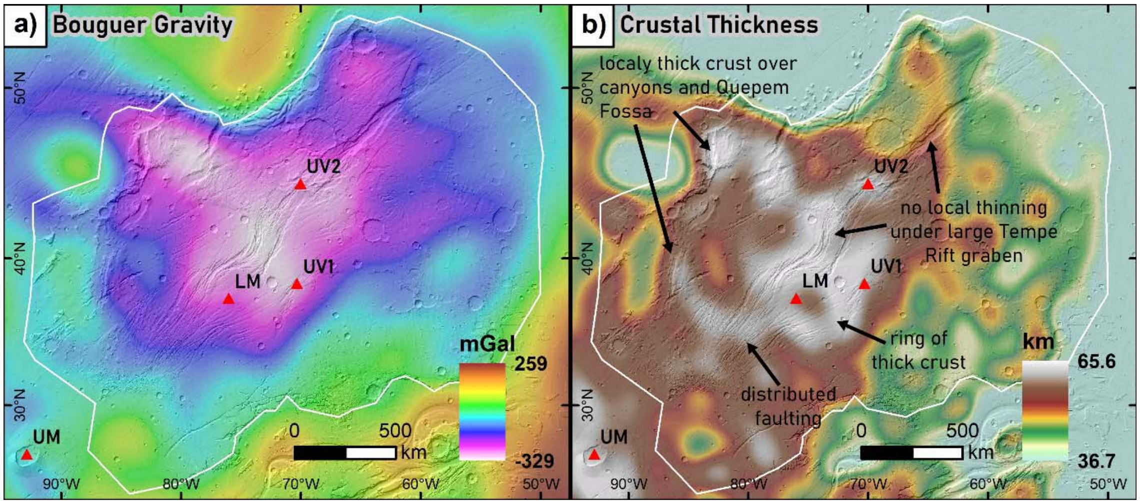

4 Discussion

4.1 Assessing fault patterns in the presence of reactivation and other complicating factors

It is difficult to determine the origin of faults from their surface expression when that surface expression no longer reflects just their initial formation mechanism. This obscuring of original conditions can result from post-tectonic modification (e.g. via erosion, mass wasting, or ice-related processes), burial of earlier structures by lava, which is particularly prevalent for Noachian structures around Tharsis, and reactivation of faults during later tectonic activity. Such effects are observed for every tectonic stage, with Stage 1 being affected most strongly by modification, burial, and reactivation (Figure 6a–d), Stage 2 by burial and reactivation (Figure 6e, f), and Stage 3 by modification and burial.

Throughout the structural evolution of Tempe Terra there is a high likelihood of extensive fault reactivation due to the similar stress state (type and orientation) through time. This long-lived stress stability, with only small, progressive changes in orientation through time, means there are increased opportunities for fault reactivation (Morris et al., 2016). Planets with a one-plate lithosphere such as Mars could be more prone to this kind of relative stress stability given the reduced crustal movement and increased surface preservation in the absence of plate tectonics. A lack of plate motions means stresses from the growing load of Tharsis and/or a stable mantle plume can continue to accumulate over the same areas of lithosphere over geologically long time periods.

The total displacement associated with reactivated faults is a combination of both their formation and later reactivation, so any measured extension for a given tectonic stage is therefore not a fully accurate picture. However, slip and dilation tendency are only an indication of the likelihood of fault reactivation and not the magnitude of any further slip (Worum et al., 2004). For earlier stages (Stage 1 and 2), some of the calculated total extension only accumulated on the faults in later stages of activity, resulting in higher extension values than the initial conditions produced. For later stages (Stage 2 and 3), some of the total extension that should be attributed to that tectonic activity is not counted as it was accumulated on pre-existing faults, resulting in lower values of extension than truly occurred. These complexities ultimately makes it difficult interpret patterns of extension where reactivation has been widespread.

4.2 Origin of Tempe Terra's observed fault patterns

By comparing the results outlined above with the expected evidence of different sources from Table 1, we first discuss which suggested models are supported or not by observations for each of Tempe Terra's tectonic stages. We subsequently present a conceptual model for the origin of the observed structural features.

4.2.1 Stage 1: Local magmatic underplating with associated heating and uplift

Most notable for Stage 1 is the lack of geometric relationships to Tharsis trends or alignment with any of the proposed Tharsis development models (Table 2; Figure 2a). This indicates the extension recorded in Tempe Terra during Stage 1 predates regional stresses from the growth of the Tharsis Rise in this region. The predominantly N orientation of structures implies Tempe Terra underwent E–W extension, and observations support volcanic uplift, magmatic underplating, dyke intrusion, or gradients of gravitational potential energy (GPE) as potential origins of this extension. Given the location of Stage 1 structures relative to the highland–lowland dichotomy boundary, N–S faults could be favoured by pre-existing fractures or damage zones radiating from the Borealis Basin, a massive impact interpreted to have formed the northern lowlands (Andrews-Hanna et al., 2008; Frey & Schultz, 1988; Wilhelms & Squyres, 1984). A direct impact origin is not supported by our observations, but earlier in Mars's history the resulting damage to the crust could have had a stronger influence in the form of structural inheritance (Schultz, 1984), before stresses and volcanic material from Tharsis eclipsed this effect.

Local magmatism appears to have played an important role in this stage, either as the driving force for extension or as a facilitating mechanism for strain localisation and lithosphere weakening. This magmatic activity is indicated in local surface features and topography. Firstly, the Tanais Fossae canyon system (Figure 2b), which aligns with Stage 1 faults, may have formed as a result of collapse after magma withdrawal or from ground ice melting or sublimating due to magmatic heating (Moore, 2001). A similar mechanism was proposed for the formation of Valles Marineris (McKenzie & Nimmo, 1999). The shape, scale and alignment of the canyons could indicate they have a structural origin and may have originally formed as graben during this tectonic stage, although this does not preclude later modification by the suggested magmatic processes. If we include the Tanais Fossae canyon system as past extensional structures, then Stage 1 could represent an early rift system that extends over 900 km. This was first interpreted by Hauber et al. (2010) as the "X-rift", and they assessed it as compatible with far-field stresses related to GPE but not Tharsis. The concentration of heave into large graben (Figure 2e) supports the rift interpretation, and local heating, such as from magmatic intrusions or underplating, could result in strain partitioning and produce the narrow rift geometry we observe (Buck, 2007). A similar localisation by magmatism and associated lithospheric weak zones is interpreted to be responsible for the Thaumasia Double Rift, which is also oriented tangential to Tharsis and does not reflect circumferential stresses related to the growth of the Tharsis Rise (Grott et al., 2007). The variation in the way extension is accommodated could also suggest local heterogeneity in crustal properties in the context of rifting – especially as the area with distributed fault heave is in the same location for both Stage 1 and Stage 2.

The narrow, linear ridges on the exposed Late Noachian units (Figure 2c) were proposed as possible dykes that were formed by injection of lava into vertical conjugate fractures (Moore, 2001). These dykes were later exposed by erosion during a fluvial resurfacing event that predates the main NE-trending faulting in Tempe Terra (Frey & Grant, 1990; Moore, 2001). This exposure through widespread erosion suggests the dykes cannot be associated with later stages of magmatectonic activity, as the crisp preservation of the graben, which also cross-cut the ridges (Figure 2c), suggest the faults have not been subject to the same modification. With variable graben dimensions, no convex graben flank uplift (Figure 3a), and non-uniform accommodation of extension (Figure 2e), Stage 1 lacks many of the indicators of dyke intrusion as the main driver of graben formation (Table 1). The visible dykes therefore act more as an indication of local magmatic activity that was contemporaneous with Stage 1. The correlation between the orientation of these exposed dykes and the graben could indicate the same fracture set is controlling the alignment of these structures, particularly for patches of NW-oriented faulting which are oblique to the primary extension direction. The initial formation of the irregular fracture pattern could reflect doming from volcanic or magmatic uplift (Carr, 1974) or, given the associated fluvial resurfacing, aqueous fluid pressure driven by heating from magma intrusion (Table 1).

Faults being concentrated where topography is high may be a simple matter of preferential preservation, but such a concentration if true could be the result of remnant uplift from local magmatic activity that concentrated stress in these zones. Faulted and uplifted regions may therefore give an indication of the extent of this magmatic activity. The presence of thickened crust in the same areas as this permanent topographic uplift could suggest magmatic underplating (Table 1). The thick crust over the deep Quepem Fossa graben (Figure 7b), as well as Tanais Fossae, would therefore indicate underplating provided magmatic compensation of any crustal thinning due to extension, a phenomenon observed at some rifts on Earth (Thybo & Artemieva, 2013; Thybo & Nielsen, 2009). The presence of a local magma source underlying the faulted zones in western Tempe Terra is further supported by the presence of the Early Noachian volcano UV2 (Figure 2a, Figure 4c), which suggests volcanic activity was already ongoing in this region in the Noachian. There is striking similarity in timing and morphology between UV2 and a system of 43 small, Early–Middle Noachian volcanic constructs identified around the southern margin of Tharsis (Xiao et al., 2012). This timing suggests they may be part of the same widespread early volcanic system, that produced numerous small shields and fissure volcanism, which is proposed as an incipient stage of Tharsis development before the main-stage centralised volcanism which produced the Tharsis Rise (Werner, 2009; Xiao et al., 2012). This distributed system of volcanoes throughout the Noachian provides a possible source for underplated magmatic material in western Tempe Terra. The areas around Quepem Fossa and Tanais Fossae are also visually similar to a subset of Noachian volcanic edifices which have been modified by tectonic deformation and may result from fissure-central eruptions (Xiao et al., 2012).

A non-magmatic origin for the observed relationship between faults and elevated topography is also possible. The concentration of extensional faults in regions of high topography, and parallel to the trend of these elevated zones, is also evidence of stresses from horizontal gradients of GPE (Table 1; Molnar & Lyon-Caen, 1988) – as long as these areas were also elevated at the time of faulting. However, this gravity spreading from GPE typically needs to be facilitated by a sufficiently warm and therefore weak lithosphere and/or the presence of a detachment surface or ductile layer (Schultz-Ela, 2001; Sonder et al., 1987). Jones et al. (1996) calculated GPE was capable of producing significant strain rates in the Basin and Range Province in southwestern USA when coupled with a sufficiently weak lithosphere. Locally warm and weak lithosphere could be facilitated by the higher heat flux and thermal gradients on Mars during the Noachian (Broquet & Wieczorek, 2019; McGovern et al., 2002, 2004) or through the presence of a magmatic centre under western Tempe

Terra due to underplating. Intrusions of hot material from such magmatic underplating could also help sustain the extension for longer (Molnar & Lyon-Caen, 1988). Alternatively, the presence of subsurface salt, such as Montgomery et al. (2009) proposed for the Thaumasia Plateau region, could provide the requisite low-strength layer. A significant negative anomaly in the Bouguer gravity over Tempe Terra (Figure 7a) is consistent with accumulation of lower density material, which could include salt.

Preservation bias and the extensive reactivation of N–S faults during Stage 2 (Figure 6a, b), as well as potential further reactivation during Stage 3 (Figure 6c, d), has added additional complexity to the interpretation of this stage. Reactivation has likely contributed to the apparently Early Hesperian age of some faults, despite the bulk of tectonic activity occurring in the Noachian. While the original scope of structural activity was probably more extensive than what is preserved, the lack of structures in the eastern half of the plateau – where we would likely see some structures preserved due to the lack of younger cover were they present in the first place – suggests Stage 1 tectonic activity was still contained to the west of Tempe Terra. Ultimately, we do not have enough information to completely narrow down the origin of faults in this stage, but we present one plausible model in section 4.2.4.

4.2.2 Stage 2: Far-field regional stress and local magmatism along the Tharsis Montes Axial Trend

The defining feature of Stage 2 evolution is the combination of regional and local sources to create the complex fault patterns of the Tempe Rift, with multiple local volcanic sources interacting with regional far-field stress. The fact that structures are radial to Tharsis and concentrated along the Tharsis Montes Axial Trend suggests a genetic link between these features, which has been suggested in past studies of Tempe Terra (Fernández & Anguita, 2007; Hauber & Kronberg, 2001; Tanaka et al., 1991). In particular, the clear alignment of the rift axis to the Tharsis Montes Axial Trend (Figure 4a) indicates that this trend has played a significant role in controlling and localising tectonic activity in Stage 2.

The Tempe Rift is interpreted to be a product of sinistral oblique rifting caused by the interaction of a zone of weakness along the Tharsis Montes Axial Trend with local heterogeneities, reactivation of Stage 1 structures, and regional far-field stresses (Fernández & Anguita, 2007; Orlov et al., 2022). Rift axis-parallel faults reflect the localising effect of the Tharsis Montes Axial Trend, while rift-oblique faults reflect the far-field stress and are orthogonal to the oblique extension direction (Fernández & Anguita, 2007; Orlov et al., 2022). This indicates that the regional extension direction was ESE–WNW, despite the NE orientation of the rift axis. The trend of these extension-orthogonal faults traces back to Syria Planum (Figure 4a, purple arrow), an uplifted region in the south of Tharsis (Figure 1a) proposed to be an early centre for Tharsis growth (Anderson et al., 2001). The far-field stress is therefore likely related to growth of the Tharsis Rise topographic bulge and main-stage Tharsis volcanism. The regional decline in elevation from SW to NE across Tempe Terra forms part of this topographic bulge (Figure 4a), and the increase in total extension with proximity to the centre of Tharsis (Figure 4e), also observed by Golombek et al. (1996), could reflect higher stress closer to the source (i.e. Tharsis) (Cailleau et al., 2003). The subparallel radial relationship of rift-oblique faults to the Syria Planum centre supports several modes of Tharsis development (flexural loading, isostatic compensation, detached crustal cap; Table 2), as well as volcanic uplift (i.e. Tharsis plume) or injection of a dyke swarm as potential origins (Table 1; Table 2). There is currently a mismatch between the orientation of Stage 2 extension and the stress trajectory models for Tharsis (Table 2; Figure 4a), as the central point for these models is located at the Tharsis Montes rather than Syria Planum.

Since the majority of the Tharsis Montes Axial Trend is defined by volcanic features, including volcanic centres within Tempe Terra itself, it stands to reason that the trend can be considered a linear zone of high magmatic activity – regardless of the underlying mechanism for its linear nature (discussed in section 4.3). This magmatic zone could have weakened the lithosphere through heating and initiated and concentrated extension into a narrow rift (Buck, 2007; Hauber et al., 2010; Tanaka et al., 1991). This strain localisation is reflected in the uneven distribution of fault heave (Figure 4f). Regional domal uplift over a mantle plume, and associated volcanism, has been proposed as the mechanism for the development of the Tempe Rift (Hauber & Kronberg, 2001). Volcanic uplift over a local plume is supported by the elevated topography around the rift, the low density anomaly in the Bouguer gravity (Figure 7a), and the presence of three intra-rift volcanic centres (Labeatis Mons, UV1, UV2; Figure 4a–c; Table 1). However, the Tempe Rift faults do not have the characteristic radial pattern expected with uplift, nor the hourglass pattern associated with uplift in a regional extensional stress field (Table 1). Therefore, rather than a volcanic uplift model, a plume may instead have produced local magmatic underplating and formed a single, NE-oriented magma reservoir or a series of magma bodies along the Tharsis Montes Axial Trend which fed the local volcanoes. The lack of local crustal thinning under the Tempe Rift (Figure 7b) suggests the Moho is relatively flat beneath the large rift graben, indicating crustal thinning during rift formation may have been compensated by such magmatic underplating (Table 1). Together, these sources could have contributed to oblique rifting by providing heating and uplift that weakened the crust and helped initiate faulting in conjunction with regional stresses from Tharsis to create a complex pattern of extensional structures, an effect also observed at Alba Mons (Cailleau et al., 2003; Cailleau et al., 2005). The magmatism responsible for Stage 1 activity does not exert spatial control on Stage 2 faulting so it possibly cooled as magma became localised along the Tharsis Montes Axial Trend. This localisation is consistent with a gradual transition from widespread, plain-style volcanism to more mantle plume-controlled, Tharsis-central volcanism from the Late Noachian to Late Hesperian (Xiao et al., 2012).

It is also possible that a system of dykes was involved in forming some graben given the underlying magmatic zone, either propagating vertically from a magma body below or propagating laterally along the Tharsis Montes Axial Trend. Hauber et al. (2010) interpreted the linear ridges near the Tempe Rift (Figure 4d) as exposed dykes, and the accompanying collapse depression as a result of magma withdrawal. However, Stage 2 lacks other observable evidence of widespread dyke intrusion, such as the expected convex flank uplift (Figure 3b), uniform dimensions, continuous trends, or consistent alignment perpendicular to the direction of minimum compressive stress (Table 1). This lack of surface evidence may indicate that the signature of any putative dykes here has been lost in the scale of the localised extension and effects of general magmatic heating, or that dykes were not the driving force behind tectonic activity.

Superimposed on this regional system are the effects of local volcanic sources. The intra-rift volcanoes UV2, UV1, and Labeatis Mons were active pre- to syn-rift, syn-rift, and syn- to post-rift respectively (Hauber & Kronberg, 2001; Mège & Masson, 1996a). The effect of UV2 on the structures of Stage 2 is unclear but it has been heavily modified by the rift (Figure 4c). The hourglass pattern of faults centred on UV1 (Figure 4b), along with local doming and association with Tempe Terra's negative gravity anomaly (Figure 7a), indicates volcanic uplift has been a source of local graben formation in this area (Table 1; Mège et al., 2003). However, the largest structural effects are related to Labeatis Mons at the centre of the rift. The circumferential pattern of arcuate faults around the edifice (Figure 4b), which, when combined with the Tempe rift, forms a smaller scale version of the wristwatch pattern observed at Alba Mons and modelled by Cailleau et al. (2003), is suggestive of volcanic deflation in a regional extensional stress field (Table 1). The combination of this circumferential faulting with the concentric topographic trough around the edifice (Figure 4b) supports some combination of local volcanic loading and deflation as the origin for these structures (Table 1).

4.2.3 Stage 3: Lateral dyke propagation from a Tharsis plume under far-field regional stress

The correlation between Stage 3 faults and various stress models for the development of Tharsis (Table 2) suggests this stage is genetically related to the growth of the Tharsis Rise, and that regional far-field stresses played an important role in controlling the location of tectonic activity. The lack of relationship between Stage 3 faults and the Tharsis Montes Axial Trend, which had such a major role in Stage 2 activity, indicates that by this time its localising influence had ceased or been overpowered by other sources of stress. The widespread occurrence of graben across Tempe Terra (Figure 5a), along with the more uniform accommodation of extension reflected in the spatial distribution of heave between faults (Figure 5f), suggests Stage 3 lacks the kind of local magmatic zone and accompanying heating effect which dominated earlier stages. The ENE orientation of structures implies the local extension direction for Tempe Terra was SSE–NNW, and observations support regional volcanic uplift (plume), flexural loading, isostasy, dyke intrusion, and aqueous fluid pressure as potential origins of this extension (Table 1).

While regional far-field stresses were important during Stage 3 tectonic activity, a range of evidence indicates that dykes were widespread and likely the catalysts for graben formation within this background stress environment. The continuous linear trends formed by graben (Figure 5a), with convex flank uplift (Figure 3c) and consistent along-strike dimensions that cut through all terrain types (Figure 5a), are indicative of dykes (Table 1). These linear trends are also perpendicular to the minimum compressive stress predicted by the Tharsis models (Table 2), and are aligned with linear and volcanic surface features that further support a dyke interpretation (Figure 5b–d). The pit crater chains, which are most strongly correlated with Stage 3 (Figure 5b), are an indication of subsurface dilation and could be related to stress from aqueous fluid pressure, dykes, or dilational normal faults and fractures (Wyrick et al., 2004). However, in the context of the other surface evidence for volcanic activity along the same trends (e.g. lines of vents) it is plausible that dykes are the cause of that dilation.

The system of dykes at Tempe Terra is similar in scale to the Mackenzie Dyke Swarm in northern Canada (~1900 km and 2200 km long, respectively) and may represent one branch of a radiating dyke swarm centred on Tharsis (Ernst et al., 2001; Mège & Masson, 1996a; Tanaka et al., 1991). A Tharsis-centred dyke swarm suggests lateral propagation over large distances (1000s of kilometres) from the source (Ernst et al., 2001), which is reflected in the total extension decreasing towards the far eastern edge of Tempe Terra (Figure 5e). There was also continued tectonic activity while volcanism was ongoing, as indicated by the faults being buried by, and then propagating through, overlying volcanic flows in the west of Tempe Terra (Figure 5a; Orlov et al., 2022). The dykes themselves could have acted as feeders for these volcanic flows that cover much of central Tharsis (Plescia, 1981). The continued tectonic activity could reflect different pulses of dyke activity or several subswarms. The variation in the width of the linear graben systems across Tempe Terra could also suggest several pulses of dyking, resulting from variations in the size of these dykes. Later pulses of activity may have waned over time as the youngest graben do not reach as far, only appearing at the western edge of Tempe Terra (Figure 1d).

The magmatic source for the dykes would have existed within Tharsis, but the lack of radial relationships to any of the main volcanic edifices indicates these are unlikely the source. The compatibility between Stage 3 faults and the Mège and Masson (1996a) Tharsis mantle plume model (Figure 5a; Table 2) provides a plausible origin for the dyke swarms. High magmatic pressures could allow for dykes to travel the far distance from a Tharsis-centred plume to Tempe Terra or other distal locations (Tanaka et al., 1991). An active plume under Tharsis was also suggested by Broquet and Wieczorek (2019) for their gravity models of the Tharsis Montes volcanoes. Such a plume may have been the source of the far-field stress in Tempe Terra if it were responsible for the growth of the Tharsis bulge (as proposed by Mège and Masson (1996a)), or it may have acted only as the magma source for the dykes as Tempe Terra was subject to other Tharsis-related stresses.

4.2.4 Conceptual model for Tempe Terra's magma- and volcanotectonic evolution

Based on the observations and discussion above, we present our interpretation for the origin of the fault system at Tempe Terra through time, which is summarised in Figure 8. Volcanic activity began in Tempe Terra in the Early Noachian, as part of an early stage of widespread volcanism in the Tharsis region which predates regional circumferential stress from large scale growth of the Tharsis Rise. In the Middle to Late Noachian (Stage 1), local magmatic underplating and associated heating and uplift in western Tempe Terra weakened the lithosphere and formed a N-oriented rift system (Figure 8a). Vertical fractures above the magma intrusion provided pathways for dyke injection and controlled the alignment of NW-oriented faults. Stage 1 structures therefore represent the effects of local sources of stress without relationship to the evolution of the Tharsis Rise.

In the Early Hesperian (Stage 2), magmatic activity was localised along the Tharsis Montes Axial Trend as the previous magmatic centres cooled and volcanism became centralised to larger Tharsis mantle plumes. This NE-trending magmatic activity interacted with ESE–WNW extension from a regional stress regime from the growth of the Tharsis Rise, centred on Syria Planum, to create oblique rifting in Tempe Terra (Figure 8b). Underplated magmatic material and a system of vertically-propagating dykes weakened the lithosphere and acted as a locus for extension, controlling the axis of the Tempe Rift and its parallel fault trend, as well as acting as a source for the intra-rift volcanoes. While rifting was ongoing, volcanic loading and deflation around Labeatis Mons produced local circumferential faults and the wristwatch graben pattern at the centre of the rift, while volcanic uplift under UV1 produced an hourglass fault pattern in a small section of the rift. Stage 2 structures therefore represent a combination of local and regional, Tharsis-related sources of stress.

From the Early to Late Hesperian (Stage 3), a series of laterally-propagating dyke swarms from a Tharsis-centred plume produced an extensive system of graben across Tempe Terra (Figure 8c). This system of dykes occurred within a regional stress field related to the growth of the Tharsis Rise, but with a centre located further north than in Stage 2. This regional stress regime produced SSE–NNW extension within Tempe Terra, which primarily controlled dyke and graben orientations as the localising effect of magmatism along the Tharsis Montes Axial Trend waned. Dyke injection was made up of a series of pulses and continued while major Tharsis volcanism was ongoing, causing faults to propagate through overlying volcanic flows in some areas. Stage 3 structures therefore represent the effects of a regional, magmatectonic, Tharsis-centred source of stress.

Figure 8: Conceptual models of the origin of tectonic stages in Tempe Terra. **a)** Stage 1 formation by local magmatic underplating predating regional influence from Tharsis. **b)** Stage 2 formation by oblique rifting from localisation along a magmatic zone on the Tharsis Montes Axial Trend and regional stress from growth of Tharsis. **c)** Stage 3 formation by laterally-propagating dyke swarms from a Tharsis-centred plume.

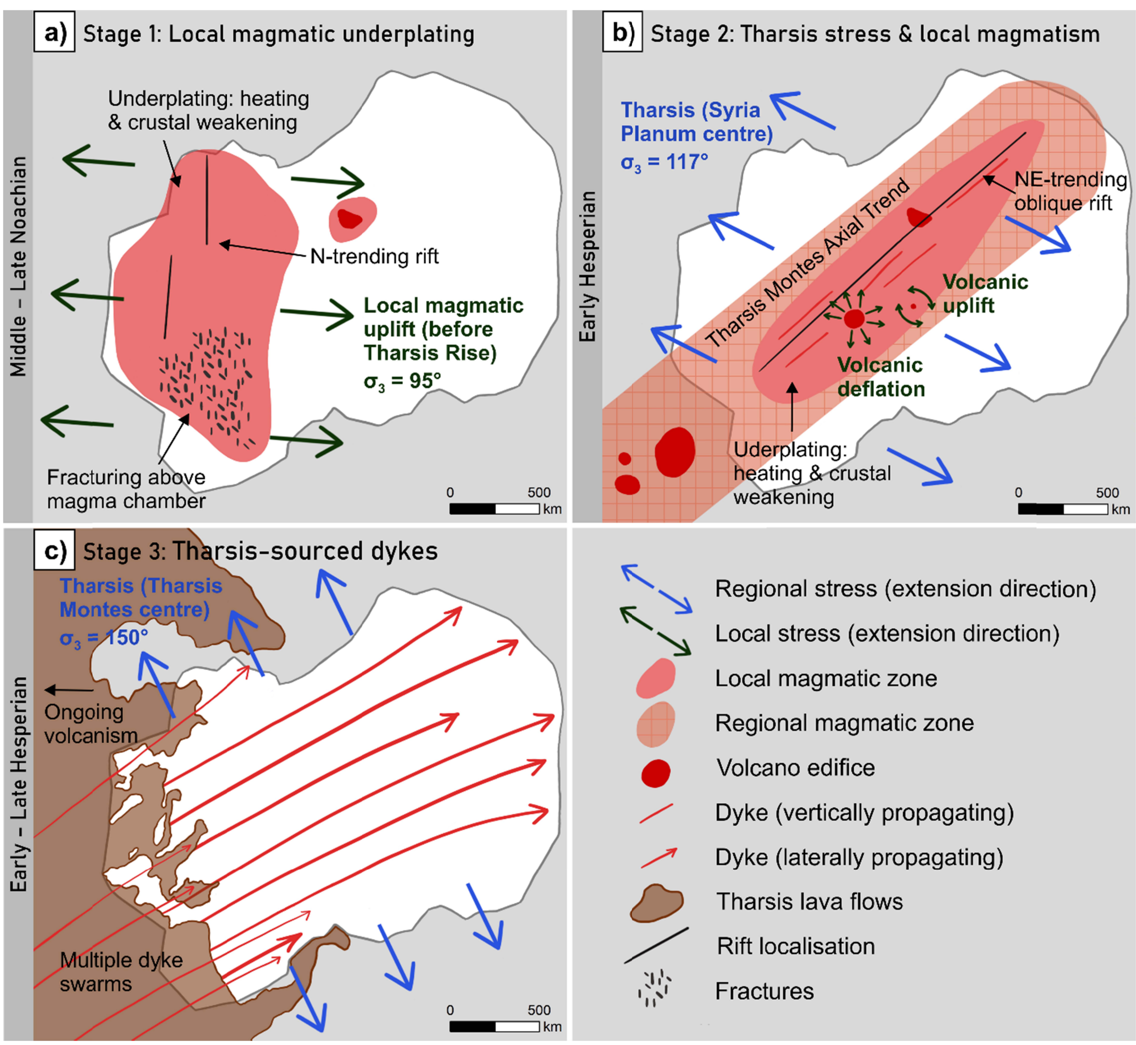

4.3 Volcanism and potential origins of the Tharsis Montes Axial Trend

The linear alignment of the Tharsis Montes and other volcanoes and structures that make up what we refer to as the Tharsis Montes Axial Trend (Figure 1a), has been a recognised feature of the Tharsis Rise since early investigations of Martian tectonics (e.g. Carr, 1974; Wise et al., 1979). Over the intervening decades several hypotheses have been proposed for the underlying mechanism controlling this linear trend. The most common model involves a zone of weakness and fracturing (Crumpler & Aubele, 1978; Hauber & Kronberg, 2001; Wise et al., 1979) or a bisecting rift zone (McGovern & Solomon, 1993) beneath the Tharsis Montes which has controlled the location of volcanism. This fracturing may be the result of a monocline formed by asymmetric mantle convection (Carr, 1974) or stress concentration along the crustal dichotomy boundary (Wise et al., 1979). Other proposed mechanisms include volcanism concentrated along the edge of an impact basin (Schultz, 1984), a migrating mantle plume (Leone, 2016), and a subduction zone with island arc volcanism in a Martian plate tectonics regime (Sleep, 1994; Tanaka, 1990). All of these scenarios remain speculative and require further investigation via approaches such as numerical modelling.

There is a progression in age and size between the volcanic centres of the Tharsis Montes Axial Trend, from older and smaller volcanoes at the edges to younger and larger volcanoes towards the centre. This trend in volcano ages has also been explored in the context of a migrating mantle plume hypothesis (Leone, 2016; Leone et al., 2022), but this model is unable to explain the inward trend of ages along the Tharsis Montes Axial Trend. From the northeast extent of the trend at Tempe Terra there is first the Early Noachian pre-rift volcano UV2 (Tanaka et al., 2014), then the Early Hesperian-aged Labeatis Mons (Hauber & Kronberg, 2001), the Late Hesperian Uranius Mons Group volcanoes (Plescia, 2000), and finally the three Amazonian-aged Tharsis Montes (Robbins et al., 2011). Although the trend is less obvious on the southeast side of the Tharsis Montes towards Terra Sirenum, the same inward age and size progression is present. At the furthest extent of the trend is the Early Noachian Sirenum Mons (Xiao et al., 2012), followed by the Early–Middle Noachian Sirenum Tholus (Xiao et al., 2012), which is the same ~2000 km distance from the Tharsis Montes as Labeatis Mons (Figure 1a). These ages refer to the last activity of the volcano (i.e. surface age) and not necessarily the development of the edifice itself. This trend in active volcanism could reflect a progressive cooling or loss of magma supply which meant volcanic centres at the edges of the Tharsis Montes Axial Trend could not grow as large and their activity stopped earlier.

This pattern of volcanic activity along the Tharsis Montes Axial Trend is consistent with a transition from an incipient Tharsis volcanic province with widespread small volcanoes, to larger, focused, mantle plume-driven volcanism which produced the topographic bulge and major volcanoes of the Tharsis Rise (Werner, 2009; Xiao et al., 2012). The alignment of the Noachian volcanic edifices at UV2 and Terra Sirenum indicate that the underlying structure controlling the Tharsis Montes Axial Trend was in place during the initial Early Noachian volcanic period, predating development of the main Tharsis Rise. However, this structure did not exert a major control on tectonic activity until magma became highly localised along the trend in the Late Noachian–Early Hesperian. Further consolidation of that magma within central Tharsis later in the Hesperian could be why a shift is observed from faulting aligned with the Tempe Rift and Tharsis Montes Axial Trend in Stage 3. As active heating and extension controlled by magma supply under Tempe Terra reduced, an injection of dykes from the now more centralised plume could cut through, forming new faults rather than only reactivating pre-existing ones despite the similarity in stress field. Ultimately, our results provide evidence for the timing of the Tharsis Montes Axial Trend but cannot determine the mechanism controlling the trend.

4.4 Implications for models of Tharsis development

Our findings have implications for models of both the mechanism and timing of development of the Tharsis Rise. In terms of formation mechanism, we can clarify and focus the criteria for plausible formation models for Tharsis. The complex faulting in Tempe Terra is a combination of overprinted regional and local patterns. Many of the fault sets can therefore be put aside when evaluating models of Tharsis's tectonic evolution – either because they predate Tharsis, they reflect local processes, or they relate to specific causes such as magmatism along the Tharsis Montes Axial Trend. Given the complexity of structural features associated with Tharsis in many areas, having subsets of faults which reflect local processes is also likely to be true elsewhere. For Tempe Terra, there are only two far-field stress regimes which relate to growth of the Tharsis Rise: one that produced NNE-trending, rift-oblique faults in Stage 2; and one that produced ENE-trending faults in Stage 3. These are therefore the only regional fault trends that Tharsis models need to match in Tempe Terra. Of the models compared here, the fault trends of Stage 3 are better reproduced than those of Stage 2 (Table 2), indicating a gap in these predictions of Tharsis-derived stresses.

There is the potential to simplify our criteria for models of Tharsis development if we utilise the range of detailed geological studies on specific regions (e.g. Anderson et al., 2019; Cailleau et al., 2005; Kling et al., 2021) to identify structures that reflect only local volcanic, magmatic, and tectonic activity, and remove these from future regional tectonic analyses. Doing so would make it easier to see the regional trends relevant to the large-scale processes involved in Tharsis's development, which is made substantially more complex where it interacts with the variety of local processes also at play.

In terms of the timing of Tharsis's development, our results support the idea of long-lasting volcanism in the Tharsis region (Early Noachian to Amazonian), but a later (Early Hesperian) development of the deformation resulting from the large scale growth of what we now consider the Tharsis Rise (i.e., the topographic bulge and main-stage volcanism which produced the five major Tharsis volcanoes). Stage 1 in Tempe Terra predating main-stage Tharsis activity supports this later evolution compared to some earlier models (e.g. Anderson et al., 2001; Phillips et al., 2001), and we see an increasing role of regional, Tharsis-related stresses as local magmatism within Tempe Terra wanes and development of the Tharsis Rise begins. This Early Hesperian age for development of the Tharsis Rise is supported by proposed Tharsis-driven true polar wander during the Early–Late Hesperian period (Bouley et al., 2016). However, Tempe Terra's location at the periphery of Tharsis means it could have experienced the regional stresses from the growth of Tharsis later than more central locations on the Rise, and therefore initial Tharsis activity may have been underway elsewhere in the Late Noachian. A Late Noachian–Early Hesperian development for Tharsis has been proposed previously (e.g. Bouley et al., 2016; Bouley et al., 2018; Tanaka et al., 1991) but we include in our interpretation a precursor period of distributed volcanism and development of the Tharsis Montes Axial Trend as early phases in the evolution of the Tharsis region.

5 Conclusions

We compared surface observations of tectonic stages in Tempe Terra with predicted structural outcomes for different formation hypotheses to determine the origin of extensional structures through time. Our interpretations are complicated by the effects of fault reactivation, burial, and post-tectonic modification, particularly for earlier stages, but we make the following conclusions:

- Each of the three stages of tectonic activity in Tempe Terra have a different origin which has influenced their expression, with a combination of local and regional magmatic sources being the cause of faulting in each stage.
- Middle to Late Noachian Stage 1 faulting was the result of local magmatic underplating and associated heating and uplift in western Tempe Terra. Extension from these local sources of stress produced an early N-oriented rift system which predates development of the Tharsis Rise.
- Early Hesperian Stage 2 faulting was produced by the interaction of local magmatic activity along the Tharsis Montes Axial Trend with far-field regional stresses from the growth of the Tharsis Rise. The combination of these effects with local stresses from intra-rift volcanoes created NE-oriented oblique rifting.
- Early to Late Hesperian Stage 3 faulting was the result of a series of laterally-propagating dyke swarms from a Tharsis-centred plume, which formed in a far-field regional stress field related to the growth of the Tharsis Rise.

- The Tharsis Montes Axial Trend has been present since the Early Noachian, forming during an early phase of widespread volcanism in the Tharsis region, but prior to growth of the topographic bulge and centralised volcanism of the Tharsis Rise.
- Our findings support a Late Noachian–Early Hesperian development of the Tharsis Rise and provide clearer criteria for Tharsis formation models in terms of their expression in Tempe Terra. Only two fault orientations (NNE in Stage 2 and ENE in Stage 3) reflect Tharsis-related regional stresses and need to be reproduced by regional models, while the rest of the faults can be put aside for these assessments.
- Our study shows that utilising a similar process that focuses on isolating regional trends from other areas across Tharsis has the potential to provide not only improved criteria for evaluating models of Tharsis development in the future, but also could prove valuable when assessing complicated surface features on planetary bodies generally.

Acknowledgements

This work was supported by the University of Leeds International Doctoral Scholarship. Thank you to Maeve Murphy Quinlan for her invaluable assistance in testing various code-based approaches in the course of this study. We are grateful to NASA and ESA for making Mars data freely available through NASA's Planetary Data System (PDS).

Data Availability Statement

The catalog of mapped structural features used in this work is available for download in shapefile format from Zenodo (Orlov, 2022). HRSC images and DEMs and CTX images can be downloaded from NASA's PDS Geoscience Node: HRSC (European Space Agency, 2022 and https://pds-geosciences.wustl.edu/missions/mars_express/hrsc.htm), CTX (Malin, 2007 and https://pds-imaging.jpl.nasa.gov/portal/mro_mission.html). The MOLA-HRSC global DEM (Version 2) can be downloaded from the USGS Astropedia Catalog (Fergason et al., 2018 and http://bit.ly/HRSC_MOLA_Blend_v0). The Goddard Mars Model–3 Bouguer gravity and crustal thickness models are available from the PDS Geoscience Node (Genova et al., 2016 and https://pds-geosciences.wustl.edu/mro/mro-m-rss-5-sdp-v1/mrors_1xxx/data/).

6 References

Allen, P. A., & Allen, J. R. (2005). *Basin analysis: principles and applications* (Second ed.). Oxford, UK: Blackwell Publishing.

Anderson, R. C., Dohm, J. M., Golombek, M. P., Haldemann, A. F. C., Franklin, B. J., Tanaka, K. L., et al. (2001). Primary centers and secondary concentrations of tectonic activity through time in the western hemisphere of Mars. *Journal of Geophysical Research: Planets, 106*(E9), 20563-20585. https://doi.org/10.1029/2000JE001278

Anderson, R. C., Dohm, J. M., Williams, J. P., Robbins, S. J., Siwabessy, A., Golombek, M. P., & Schroeder, J. F. (2019). Unraveling the geologic and tectonic history of the Memnonia-Sirenum region of Mars: Implications on the early formation of the Tharsis rise. *Icarus, 332*, 132-150. https://doi.org/10.1016/j.icarus.2019.06.010

Andrews-Hanna, J. C., Zuber, M. T., & Banerdt, W. B. (2008). The Borealis basin and the origin of the martian crustal dichotomy. *Nature, 453*(7199), 1212-1215. https://doi.org/10.1038/nature07011

Baker, V. R., Maruyama, S., & Dohm, J. M. (2007). Tharsis superplume and the geological evolution of early Mars. In Superplumes: Beyond plate tectonics (pp. 507-522): Springer. Retrieved from https://doi.org/10.1007/978-1-4020-5750-2_16.

Banerdt, W. B., Golombek, M. P., & Tanaka, K. L. (1992). Stress and tectonics on Mars. In H. H. Kieffer, B. M. Jakosky, C. W. Snyder, & M. S. Matthews (Eds.), *Mars* (pp. 249-297). Tucson: University of Arizona Press.

Banerdt, W. B., Phillips, R. J., Sleep, N. H., & Saunders, R. S. (1982). Thick shell tectonics on one-plate planets: Applications to Mars. *Journal of Geophysical Research: Solid Earth, 87*(B12), 9723-9733. https://doi.org/10.1029/JB087iB12p09723

Barnett, D. N., & Nimmo, F. (2002). Strength of Faults on Mars from MOLA Topography. *Icarus, 157*(1), 34-42. https://doi.org/10.1006/icar.2002.6817

Bons, P. D., Cao, D., de Riese, T., González-Esvertit, E., Koehn, D., Naaman, I., et al. (2022). A review of natural hydrofractures in rocks. *Geological Magazine, 159*(11-12), 1952-1977. https://doi.org/10.1017/S0016756822001042

Bouley, S., Baratoux, D., Matsuyama, I., Forget, F., Sejourne, A., Turbet, M., & Costard, F. (2016). Late Tharsis formation and implications for early Mars. *Nature, 531*(7594), 344-347. https://doi.org/10.1038/nature17171

Bouley, S., Baratoux, D., Paulien, N., Missenard, Y., & Saint-Bézar, B. (2018). The revised tectonic history of Tharsis. *Earth and Planetary Science Letters, 488*, 126-133. https://doi.org/10.1016/j.epsl.2018.02.019

Broquet, A., & Wieczorek, M. A. (2019). The Gravitational Signature of Martian Volcanoes. *Journal of Geophysical Research: Planets, 124*(8), 2054-2086. https://doi.org/10.1029/2019JE005959

Buck, W. R. (2007). Dynamic Processes in Extensional and Compressional Settings: The Dynamics of Continental Breakup and Extension. In G. Schubert (Ed.), Treatise on Geophysics (pp. 335-376). Amsterdam: Elsevier. Retrieved from https://doi.org/10.1016/B978-044452748-6.00110-3.

Byrne, P. K., Holohan, E. P., Kervyn, M., van Wyk de Vries, B., & Troll, V. R. (2015). Analogue modelling of volcano flank terrace formation on Mars. *Geological Society, London, Special Publications, 401*(1), 185. https://doi.org/10.1144/SP401.14

Cailleau, B., Walter, T. R., Janle, P., & Hauber, E. (2003). Modeling volcanic deformation in a regional stress field: Implications for the formation of graben structures on Alba Patera, Mars. *Journal of Geophysical Research: Planets, 108*(E12). https://doi.org/10.1029/2003JE002135

Cailleau, B., Walter, T. R., Janle, P., & Hauber, E. J. I. (2005). Unveiling the origin of radial grabens on Alba Patera volcano by finite element modelling. *Icarus, 176*(1), 44-56. https://doi.org/10.1016/j.icarus.2005.01.017

Carr, M. H. (1974). Tectonism and volcanism of the Tharsis Region of Mars. *Journal of Geophysical Research, 79*(26), 3943-3949. https://doi.org/10.1029/JB079i026p03943

Corti, G., van Wijk, J., Cloetingh, S., & Morley, C. K. (2007). Tectonic inheritance and continental rift architecture: Numerical and analogue models of the East African Rift system. *Tectonics, 26*(6). https://doi.org/10.1029/2006TC002086

Cox, K. G. (1993). Continental magmatic underplating. *Philosophical Transactions of the Royal Society of London. Series A: Physical and Engineering Sciences, 342*(1663), 155-166. https://doi.org/10.1098/rsta.1993.0011

Crough, S. T. (1983). Hotspot swells. *Annual Review of Earth and Planetary Sciences, 11*(1), 165-193. https://doi.org/10.1146/annurev.ea.11.050183.001121

Crumpler, L. S., & Aubele, J. C. (1978). Structural evolution of Arsia Mons, Pavonis Mons, and Ascreus Mons: Tharsis region of Mars. *Icarus, 34*(3), 496-511. https://doi.org/10.1016/0019-1035(78)90041-6

Davis, P. A., Tanaka, K. L., & Golombek, M. P. (1995). Topography of Closed Depressions, Scarps, and Grabens in the North Tharsis Region of Mars: Implications for Shallow Crustal Discontinuities and Graben Formation. *Icarus, 114*(2), 403-422. https://doi.org/10.1006/icar.1995.1071

Dimitrova, L. L., Holt, W. E., Haines, A. J., & Schultz, R. A. (2006). Toward understanding the history and mechanisms of Martian faulting: The contribution of gravitational potential energy. *Geophysical Research Letters, 33*(8). https://doi.org/10.1029/2005GL025307

Dohm, J. M., Baker, V. R., Maruyama, S., & Anderson, R. C. (2007). Traits and Evolution of the Tharsis Superplume, Mars. In D. A. Yuen, S. Maruyama, S.-I. Karato, & B. F. Windley (Eds.), Superplumes: Beyond Plate Tectonics (pp. 523-536). Dordrecht: Springer Netherlands. Retrieved from https://doi.org/10.1007/978-1-4020-5750-2_17.

Ernst, R. E., Grosfils, E., & Mège, D. (2001). Giant Dike Swarms: Earth, Venus, and Mars. *Annual Review of Earth and Planetary Sciences, 29*(1), 489-534. https://doi.org/10.1146/annurev.earth.29.1.489

Ernst, R. E., Head, J. W., Parfitt, E., Grosfils, E., & Wilson, L. (1995). Giant radiating dyke swarms on Earth and Venus. *Earth-Science Reviews, 39*(1), 1-58. https://doi.org/10.1016/0012-8252(95)00017-5

Fergason, R. L., Hare, T. M., & Laura, J. (2018). HRSC and MOLA blended digital elevation model at 200m v2. *Astrogeology PDS Annex, US Geological Survey*. http://bit.ly/HRSC_MOLA_Blend_v0

Fernández, C., & Anguita, F. (2007). Oblique rifting at Tempe Fossae, Mars. *Journal of Geophysical Research: Planets, 112*(E9). https://doi.org/10.1029/2007JE002889

Ferrill, D. A., Smart, K. J., & Morris, A. P. (2020). Fault failure modes, deformation mechanisms, dilation tendency, slip tendency, and conduits v. seals. *Geological Society, London, Special Publications, 496*(1), 75-98. https://doi.org/10.1144/SP496-2019-7

Ferrill, D. A., Winterle, J., Wittmeyer, G. W., Sims, D., Colton, S. L., & Armstrong, A. (1999). *Stressed Rock Strains Groundwater at Yucca Mountain, Nevada*.

Frey, H. V., & Grant, T. D. (1990). Resurfacing history of Tempe Terra and surroundings. *Journal of Geophysical Research: Solid Earth, 95*(B9), 14249-14263. https://doi.org/10.1029/JB095iB09p14249

Frey, H. V., & Schultz, R. A. (1988). Large impact basins and the mega-impact origin for the crustal dichotomy on Mars. *Geophysical Research Letters, 15*(3), 229-232. https://doi.org/10.1029/GL015i003p00229

Genova, A., Goossens, S., Lemoine, F. G., Mazarico, E., Neumann, G. A., Smith, D. E., & Zuber, M. T. (2016). Seasonal and static gravity field of Mars from MGS, Mars Odyssey and MRO radio science. *Icarus, 272*, 228-245. https://doi.org/10.1016/j.icarus.2016.02.050

Golombek, M. P., & Phillips, R. J. (2010). Mars tectonics. In R. A. Schultz & T. R. Watters (Eds.), Planetary Tectonics Cambridge Planetary Science (pp. 183-232). Cambridge: Cambridge University Press. Retrieved from https://doi.org/10.1017/CBO9780511691645.006.

Golombek, M. P., Tanaka, K. L., & Franklin, B. J. (1996). Extension across Tempe Terra, Mars, from measurements of fault scarp widths and deformed craters. *Journal of Geophysical Research: Planets, 101*(E11), 26119-26130. https://doi.org/10.1029/96JE02709

Goudy, C. L., & Schultz, R. A. (2005). Dike intrusions beneath grabens south of Arsia Mons, Mars. *Geophysical Research Letters, 32*(5). https://doi.org/10.1029/2004GL021977

Grott, M., Kronberg, P., Hauber, E., & Cailleau, B. (2007). Formation of the double rift system in the Thaumasia Highlands, Mars. *Journal of Geophysical Research: Planets, 112*(E6). https://doi.org/10.1029/2006JE002800

Hauber, E., Grott, M., & Kronberg, P. (2010). Martian rifts: Structural geology and geophysics. *Earth and Planetary Science Letters, 294*(3-4), 393-410. https://doi.org/10.1016/j.epsl.2009.11.005

Hauber, E., & Kronberg, P. (2001). Tempe Fossae, Mars: A planetary analogon to a terrestrial continental rift? *Journal of Geophysical Research: Planets, 106*(E9), 20587-20602. https://doi.org/10.1029/2000JE001346

Janle, P., & Erkul, E. (1991). Gravity studies of the Tharsis area on Mars. *Earth, Moon, and Planets, 53*(3), 217-232. https://doi.org/10.1007/BF00055948

Jaumann, R., Hiesinger, H., Anand, M., Crawford, I. A., Wagner, R., Sohl, F., et al. (2012). Geology, geochemistry, and geophysics of the Moon: Status of current understanding. *Planetary and Space Science, 74*(1), 15-41. https://doi.org/10.1016/j.pss.2012.08.019

Jaumann, R., Neukum, G., Behnke, T., Duxbury, T. C., Eichentopf, K., Flohrer, J., et al. (2007). The high-resolution stereo camera (HRSC) experiment on Mars Express: Instrument aspects and experiment conduct from interplanetary cruise through the nominal mission. *Planetary and Space Science, 55*(7), 928-952. https://doi.org/10.1016/j.pss.2006.12.003

Jones, C. H., Unruh, J. R., & Sonder, L. J. (1996). The role of gravitational potential energy in active deformation in the southwestern United States. *Nature, 381*(6577), 37-41. https://doi.org/10.1038/381037a0

Kenkmann, T., Poelchau, M. H., & Wulf, G. (2014). Structural geology of impact craters. *Journal of Structural Geology, 62*, 156-182. https://doi.org/10.1016/j.jsg.2014.01.015

Klimczak, C. (2014). Geomorphology of lunar grabens requires igneous dikes at depth. *Geology, 42*(11), 963-966. https://doi.org/10.1130/G35984.1

Kling, C. L., Byrne, P. K., Atkins, R. M., & Wegmann, K. W. (2021). Tectonic Deformation and Volatile Loss in the Formation of Noctis Labyrinthus, Mars. *Journal of Geophysical Research: Planets, 126*(11), e2020JE006555. https://doi.org/10.1029/2020JE006555

Leone, G. (2016). Alignments of volcanic features in the southern hemisphere of Mars produced by migrating mantle plumes. *Journal of Volcanology and Geothermal Research, 309*, 78-95. https://doi.org/10.1016/j.jvolgeores.2015.10.028

Leone, G., Grosse, P., Ahrens, C., & Gasparri, D. (2022). Geomorphological and morphometric characteristics of the volcanic edifices along a volcanic alignment of Tharsis on Mars. *Geomorphology, 414*, 108385. https://doi.org/10.1016/j.geomorph.2022.108385

Malin, M. C., Bell Iii, J. F., Cantor, B. A., Caplinger, M. A., Calvin, W. M., Clancy, R. T., et al. (2007). Context Camera investigation on board the Mars Reconnaissance Orbiter. *Journal of Geophysical Research: Planets, 112*(E5). https://doi.org/10.1029/2006JE002808

McGovern, P. J., & Solomon, S. C. (1993). State of stress, faulting, and eruption characteristics of large volcanoes on Mars. *Journal of Geophysical Research: Planets, 98*(E12), 23553-23579. https://doi.org/10.1029/93JE03093

McGovern, P. J., Solomon, S. C., Head, J. W., Smith, D. E., Zuber, M. T., & Neumann, G. A. (2001). Extension and uplift at Alba Patera, Mars: Insights from MOLA observations and loading models. *Journal of Geophysical Research: Planets, 106*(E10), 23769-23809. https://doi.org/10.1029/2000JE001314

McGovern, P. J., Solomon, S. C., Smith, D. E., Zuber, M. T., Simons, M., Wieczorek, M. A., et al. (2002). Localized gravity/topography admittance and correlation spectra on Mars: Implications for regional and global evolution. *Journal of Geophysical Research: Planets, 107*(E12), 19-11-19-25. https://doi.org/10.1029/2002JE001854

McGovern, P. J., Solomon, S. C., Smith, D. E., Zuber, M. T., Simons, M., Wieczorek, M. A., et al. (2004). Correction to “Localized gravity/topography admittance and correlation spectra on Mars: Implications for regional and global evolution”. *Journal of Geophysical Research: Planets, 109*(E7). https://doi.org/10.1029/2004JE002286

McKenzie, D., & Nimmo, F. (1999). The generation of martian floods by the melting of ground ice above dykes. *Nature, 397*(6716), 231-233. https://doi.org/10.1038/16649

Mège, D. (1999). *Dikes on Mars:(1) What to look for?(2) A first survey of possible dikes during the Mars Global Surveyor aerobreaking and science phasing orbits.* Paper presented at the The Fifth International Conference on Mars, Pasadena, California.

Mège, D., Cook, A. C., Garel, E., Lagabrielle, Y., & Cormier, M.-H. (2003). Volcanic rifting at Martian grabens. *Journal of Geophysical Research: Planets, 108*(E5). https://doi.org/10.1029/2002JE001852

Mège, D., & Masson, P. (1996a). A plume tectonics model for the Tharsis province, Mars. *Planetary and Space Science, 44*(12), 1499-1546. https://doi.org/10.1016/S0032-0633(96)00113-4

Mège, D., & Masson, P. (1996b). Stress models for Tharsis formation, Mars. *Planetary and Space Science, 44*(12), 1471-1497. https://doi.org/10.1016/S0032-0633(96)00112-2

Molnar, P., & Lyon-Caen, H. (1988). Some simple physical aspects of the support, structure, and evolution of mountain belts. In S. P. Clark, Jr., B. C. Burchfiel, & J. Suppe (Eds.), Processes in Continental Lithospheric Deformation (Vol. 218, pp. 0): Geological Society of America. Retrieved from https://doi.org/10.1130/SPE218-p179.

Montgomery, D. R., Som, S. M., Jackson, M. P. A., Schreiber, B. C., Gillespie, A. R., & Adams, J. B. (2009). Continental-scale salt tectonics on Mars and the origin of Valles Marineris and associated outflow channels. *GSA Bulletin, 121*(1-2), 117-133. https://doi.org/10.1130/B26307.1

Moore, J. H. (Cartographer). (2001). Geologic map of the Tempe-Mareotis region of Mars [USGS Geologic Investigations Series I–2727]. Retrieved from https://doi.org/10.3133/i2727

Morris, A. P., Ferrill, D. A., & Henderson, D. B. (1996). Slip-tendency analysis and fault reactivation. *Geology, 24*(3), 275-278. https://doi.org/10.1130/0091-7613(1996)024<0275:STAAFR>2.3.CO;2

Morris, A. P., Ferrill, D. A., & McGinnis, R. N. (2016). Using fault displacement and slip tendency to estimate stress states. *Journal of Structural Geology, 83*, 60-72. https://doi.org/10.1016/j.jsg.2015.11.010

Neukum, G., Jaumann, R., & HRSC Co-Investigator and Experiment Team. (2004). HRSC: the high resolution stereo camera of Mars Express. In A. Wilson (Ed.), Mars Express : The Scientific Payload (Vol. SP-1240, pp. 17-36). Noordwijk, The Netherlands: European Space Agency. Retrieved from https://sci.esa.int/s/WEyq9YW.

Orlov, C. J. (2022). *Tempe Terra Fault Catalogue*. Retrieved from: https://doi.org/10.5281/zenodo.6531499

Orlov, C. J., Bramham, E. K., Thomas, M., Byrne, P. K., Piazolo, S., & Mortimer, E. (2022). Structural Architecture and Deformation History of Tempe Terra, Mars. *Journal of Geophysical Research: Planets, 127*(11), e2022JE007407. https://doi.org/10.1029/2022JE007407

Phillips, R. J., Zuber, M. T., Solomon, S. C., Golombek, M. P., Jakosky, B. M., Banerdt, W. B., et al. (2001). Ancient geodynamics and global-scale hydrology on Mars. *Science, 291*(5513), 2587-2591. https://doi.org/10.1126/science.1058701

Plescia, J. B. (1981). The Tempe volcanic province of Mars and comparisons with the Snake River Plains of Idaho. *Icarus, 45*(3), 586-601. https://doi.org/10.1016/0019-1035(81)90024-5

Plescia, J. B. (2000). Geology of the Uranius Group Volcanic Constructs: Uranius Patera, Ceraunius Tholus, and Uranius Tholus. *Icarus, 143*(2), 376-396. https://doi.org/10.1006/icar.1999.6259

Robbins, S. J., Achille, G. D., & Hynek, B. M. (2011). The volcanic history of Mars: High-resolution crater-based studies of the calderas of 20 volcanoes. *Icarus, 211*(2), 1179-1203. https://doi.org/10.1016/j.icarus.2010.11.012

Rubin, A. M. (1992). Dike-induced faulting and graben subsidence in volcanic rift zones. *Journal of Geophysical Research: Solid Earth, 97*(B2), 1839-1858. https://doi.org/10.1029/91JB02170

Rubin, A. M., & Pollard, D. D. (1988). Dike-induced faulting in rift zones of Iceland and Afar. *Geology, 16*(5), 413-417. https://doi.org/10.1130/0091-7613(1988)016<0413:DIFIRZ>2.3.CO;2

Schultz-Ela, D. D. (2001). Excursus on gravity gliding and gravity spreading. *Journal of Structural Geology, 23*(5), 725-731. https://doi.org/10.1016/S0191-8141(01)00004-9

Schultz, P. H. (1984). *Impact Basin Control of Volcanic and Tectonic Provinces on Mars.* Paper presented at the 15th Lunar and Planetary Science Conference, Houston, Texas.

Schultz, R. A., & Fori, A. N. (1996). Fault-length statistics and implications of graben sets at Candor Mensa, Mars. *Journal of Structural Geology, 18*(2), 373-383. https://doi.org/10.1016/S0191-8141(96)80057-5

Schultz, R. A., Okubo, C. H., Goudy, C. L., & Wilkins, S. J. (2004). Igneous dikes on Mars revealed by Mars Orbiter Laser Altimeter topography. *Geology, 32*(10), 889-892. https://doi.org/10.1130/G20548.1

Schultz, R. A., Okubo, C. H., & Wilkins, S. J. (2006). Displacement-length scaling relations for faults on the terrestrial planets. *Journal of Structural Geology, 28*(12), 2182-2193. https://doi.org/10.1016/j.jsg.2006.03.034

Schultz, R. A., Soliva, R., Okubo, C. H., & Mège, D. (2010). Fault populations. In R. A. Schultz & T. R. Watters (Eds.), Planetary Tectonics Cambridge Planetary Science (pp. 457-510). Cambridge: Cambridge University Press. Retrieved from https://doi.org/10.1017/CBO9780511691645.011.

Sleep, N. H. (1994). Martian plate tectonics. *Journal of Geophysical Research: Planets, 99*(E3), 5639-5655. https://doi.org/10.1029/94JE00216

Solomon, S. C., & Head, J. W. (1982). Evolution of the Tharsis Province of Mars: The importance of heterogeneous lithospheric thickness and volcanic construction. *Journal of Geophysical Research: Solid Earth, 87*(B12), 9755-9774. https://doi.org/10.1029/JB087iB12p09755

Sonder, L. J., England, P. C., Wernicke, B. P., & Christiansen, R. L. (1987). A physical model for Cenozoic extension of western North America. *Geological Society, London, Special Publications, 28*(1), 187-201. https://doi.org/10.1144/GSL.SP.1987.028.01.14

Tanaka, K. L. (1990). *Martian Geologic" Revolutions": A Tale of Two pricesses.* Paper presented at the Lunar and Planetary Science Conference XXI.

Tanaka, K. L., & Davis, P. A. (1988). Tectonic history of the Syria Planum province of Mars. *Journal of Geophysical Research: Solid Earth, 93*(B12), 14893-14917. https://doi.org/10.1029/JB093iB12p14893

Tanaka, K. L., Golombek, M. P., & Banerdt, W. B. (1991). Reconciliation of stress and structural histories of the Tharsis region of Mars. *Journal of Geophysical Research: Planets, 96*(E1), 15617-15633. https://doi.org/10.1029/91JE01194

Tanaka, K. L., Skinner, J. A., Dohm, J. M., Irwin III, R. P., Kolb, E. J., Fortezzo, C. M., et al. (Cartographer). (2014). Geologic map of Mars. [USGS Scientific Investigations Map 3292]. Retrieved from https://dx.doi.org/10.3133/sim3292

Thybo, H., & Artemieva, I. M. (2013). Moho and magmatic underplating in continental lithosphere. *Tectonophysics, 609*, 605-619. https://doi.org/10.1016/j.tecto.2013.05.032

Thybo, H., & Nielsen, C. A. (2009). Magma-compensated crustal thinning in continental rift zones. *Nature, 457*(7231), 873-876. https://doi.org/10.1038/nature07688

Tibaldi, A., Pasquarè, F. A., Papanikolaou, D., & Nomikou, P. (2008). Tectonics of Nisyros Island, Greece, by field and offshore data, and analogue modelling. *Journal of Structural Geology, 30*(12), 1489-1506. https://doi.org/10.1016/j.jsg.2008.08.003

Werner, S. C. (2009). The global Martian volcanic evolutionary history. *Icarus, 201*, 44-68. https://doi.org/10.1016/j.icarus.2008.12.019

Wilhelms, D. E., & Squyres, S. W. (1984). The martian hemispheric dichotomy may be due to a giant impact. *Nature, 309*(5964), 138-140. https://doi.org/10.1038/309138a0

Wise, D. U., Golombek, M. P., & McGill, G. E. (1979). Tharsis province of Mars: Geologic sequence, geometry, and a deformation mechanism. *Icarus, 38*(3), 456-472. https://doi.org/10.1016/0019-1035(79)90200-8

Worum, G., van Wees, J.-D., Bada, G., van Balen, R. T., Cloetingh, S., & Pagnier, H. (2004). Slip tendency analysis as a tool to constrain fault reactivation: A numerical approach applied to three-dimensional fault models in the Roer Valley rift system (southeast Netherlands). *Journal of Geophysical Research: Solid Earth, 109*(B2). https://doi.org/10.1029/2003JB002586

Wu, Y.-H., & Hung, M.-C. (2016). Comparison of Spatial Interpolation Techniques Using Visualization and Quantitative Assessment. In M.-C. Hung (Ed.), Applications of Spatial Statistics (pp. Ch. 2). Rijeka: IntechOpen. Retrieved from https://doi.org/10.5772/65996.

Wyrick, D., Ferrill, D. A., Morris, A. P., Colton, S. L., & Sims, D. (2004). Distribution, morphology, and origins of Martian pit crater chains. *Journal of Geophysical Research, 109*(E6). https://doi.org/10.1029/2004JE002240

Xiao, L., Huang, J., Christensen, P. R., Greeley, R., Williams, D. A., Zhao, J., & He, Q. (2012). Ancient volcanism and its implication for thermal evolution of Mars. *Earth and Planetary Science Letters, 323-324*, 9-18. https://doi.org/10.1016/j.epsl.2012.01.027

Ziegler, P. A., & Cloetingh, S. (2004). Dynamic processes controlling evolution of rifted basins. *Earth-Science Reviews, 64*(1), 1-50. https://doi.org/10.1016/S0012-8252(03)00041-2

JGR: Planets

Supporting Information for

Magmatic origins of extensional structures in Tempe Terra, Mars

C. J. Orlov[1], E.K. Bramham[1], P.K. Byrne[2], S. Piazolo[1], and M. Thomas[1]

[1]School of Earth and Environment, University of Leeds.

[2]Department of Earth and Planetary Sciences, Washington University in St. Louis.

Contents of this file

Introduction

Our supporting information includes additional text, tables, and images to provide further detail on the methods used in the paper. Text S1 provides the method and parameters used to generate the fault heave maps presented in Figures 2, 4, and 5. Text S2 provides step-by-step instructions to reproduce the slip and dilation tendency maps presented in Figure 6.

Text S1.

Method 1: Fault heave maps

To generate maps of fault heave in ArcMap 10.6, we created a dataset of points with values of individual fault heave for each of Tempe Terra's tectonic stages (combining all fault sets from each stage) and then interpolated this data using inverse distance weighted gridding to create a continuous raster. See below for method and parameters we used.

Part 1: Prepare input data

1. Create intersection points wherever a fault intersects a profile line.
    a. Use the *Intersect* tool between fault dataset and profile lines to generate points (creates new point dataset).
2. Calculate and assign heave for each fault intersection.
    a. Calculate vertical offset on each fault using cross sections and calculate heave from this value, assuming a 60° dip (see section 2.2).
    b. Populate each point with its corresponding heave value.
3. Create "dummy" points with heave of 0 in areas without faults (to prevent extrapolation outside of faulted regions during the gridding process).
    a. Use the *Create Fishnet* tool to make a grid of lines spaced 20km apart.
    b. Use the *Intersect* tool between these new lines and the profile lines to generate additional dummy points (creates new point dataset).
    c. Delete any points that occur over faulted areas (only pad areas without faults).
    d. Populate the dummy points with a heave value of 0.
4. Merge fault intersections with dummy points to create a new dataset for interpolation.
    a. Use the *Merge* tool to create a new point dataset.

Part 2: Interpolate data to create raster

1. Grid the point data into a continuous raster using inverse distance weighted (IDW) interpolation.
    a. Use the IDW (Geostatistical Analyst) tool (see Table S1 for parameters) to generate new raster dataset.

Table S1. Parameters for IDW tool in ArcGIS used to interpolate fault heave.

Parameter	**Value**
Input data (z value)	Point intersection dataset (Heave in m)
Output raster (cell size)	10 km (1 point per cell)
Power	2
Search Neighbourhood:	
Neighbourhood type	Standard
Major semiaxis	150 km
Minor semiaxis	30 km
Angle	Average fault strike (60° for Stage 3, 38° for Stage 2, 5° for Stage 1)
Max neighbours	6
Min neighbours	1
Sector type	4 sector
Weight field	None

Text S2.

Method 2: Slip and dilation tendency

To generate maps of slip and dilation tendency, we first calculated the values of slip and dilation tendency for faults with a 60° dip using **FaultKin 8** software (available for free from: https://www.rickallmendinger.net/faultkin). We then displayed this in GIS format by assigning these values to fault segments for each of Tempe Terra's tectonic stages in **ArcMap 10.6**. See below for method and parameters we used.

Part 1: Create slip and dilation tendency values for a given stress field

1. Create text file of strike/dip/rake for theoretical faults planes with strike orientations in 1° increments from 0° to 360°, all with dip 60°, rake -90 (Figure S1).
2. Import text file into **FaultKin** and display data as faults.
3. From the *Calculations* menu, under *Slip Tendency*, run the *Slip Tendency Analysis* tool (see Table S2 for parameters).
4. Save output by selecting all faults and go to *Calculations* > *Data for Selected Faults* to copy to clipboard and paste into a new **Excel** spreadsheet.
    a. NOTE: given slip/dilation tendencies are normalised to maximum value
5. Generate absolute slip/dilation tendency values in **Excel**.
    a. For slip tendency (Ts), divide the shear stress magnitude (column: shear Magn) by the normal stress magnitude (column: normal Magn)
    b. For dilation tendency (Td), use formula to calculate $Td = (\sigma 1 - \sigma n) / (\sigma 1 - \sigma 3)$
        i. σ1 and σ3 magnitudes from Table S2 – stays same for each fault
        ii. normal stress magnitude (σn) from output data (column: normal Magn) – varies for each fault

Part 2: Assign values to faults and display in GIS format

1. Open fault data from Orlov (2022) in **ArcMap** (available for free from: https://doi.org/10.5281/zenodo.6531499).
2. Use *Split Line at Vertices* tool to convert continuous faults into segments.
3. Calculate the azimuth of each fault segment.
    a. For geodesic angle use the **Tools for Graphics and Shapes** plugin for ArcGIS (available for free from: http://www.jennessent.com/arcgis/shapes_graphics.htm) with the *Spheroidal Starting Azimuth* measurement.
4. Add new fields to the shapefile for slip and dilation tendency.
5. Populate fields with absolute values from part 1 based on each segment's azimuth.
6. Colour fault segments by attribute, using the slip or dilation tendency values e.g. with high = red and low = blue.

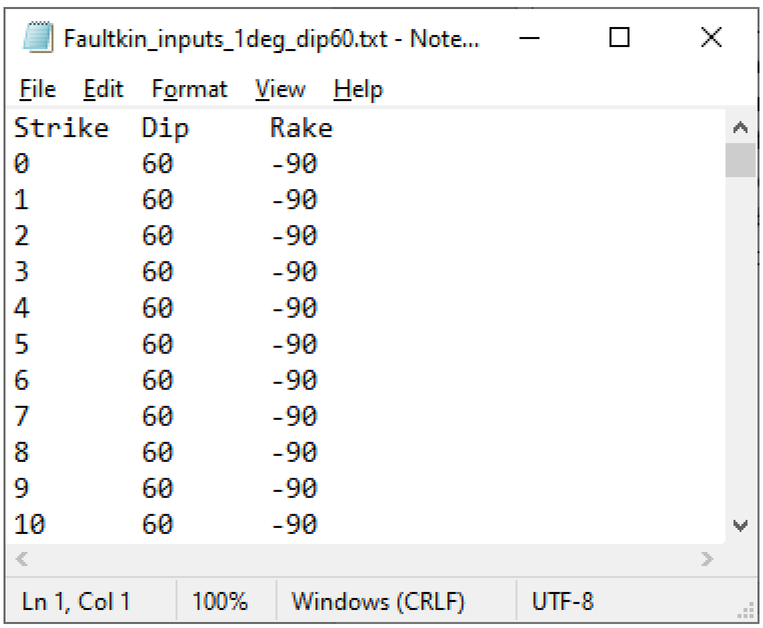

Figure S1. Example text file as input for FaultKin software.

Table S1. Parameters for slip tendency calculation in Faultkin software.

	Stage 2 Stress Regime	**Stage 3 Stress Regime**
σ1 trend	0	0
σ1 plunge	90	90
σ1 magnitude	100	100
σ2 trend	27	60
σ2 magnitude	66	66
σ3 trend	117	150
σ3 magnitude	32	32
Coefficient of static (sliding) friction[1]	0.6	0.6
Pore fluid pressure (MPa)[2,3]	0	0

[1]Schultz et al. (2006), [2]Barnett and Nimmo (2002), [3]Schultz and Fori (1996)